KUNGL
TEKNISKA
HÖGSKOLAN

Physics of
Piezoelectric Shear Mode Inkjet Actuators

Jürgen Brünahl

Stockholm 2003

Doctoral Dissertation
Royal Institute of Technology
Condensed Matter Physics

Akademisk avhandling som med tillstånd av Kungl Tekniska Högskolan framlägges till offentlig granskning för avläggande av teknisk doktorsexamen måndagen den 2 juni 2003 kl 10.00 i C1, Electrum, Isafjordsgatan 22, Kungl Tekniska Högskolan, Stockholm/Kista.

ISBN 91-628-5675-8

TRITA-FYS-5289
ISSN 0280-316X
ISRN KTH/FYS/FTS/R--03/5289--SE

© Jürgen Brünahl, 2003

Universitetsservice US AB, Stockholm 2003

Abstract

This thesis describes work on piezoelectric shear mode actuators used in drop-on-demand ink printing applications. These actuators comprise an array of ink channels micromachined into bulk $Pb(Zr_xTi_{1-x})O_3$ (PZT) ceramics.

During this study, a new pulsed spectroscopic technique was developed to investigate functional properties of a single channel wall of the actuator. The pulse technique is based on recording the transient current in response to a short voltage pulse applied to the channel wall. An electric field applied perpendicular to the polarization will cause a shear motion of the wall. If a voltage pulse with a fast rise time is high enough in amplitude to actuate the wall, it will act like a tuning fork and oscillate at it's resonant frequencies. Because of the piezoelectric effect, the mechanical oscillations of the wall can be seen as oscillations in the transient current.

Beside the pulsed technique, dielectric spectroscopy, ferroelectric hysteresis loop tracing and stroboscopy were used as characterization techniques. The results obtained are discussed in respect to temperature dependence, frequency dispersion, ferroelectric fatigue and acoustic resonance modes.

Another field of interest was the temperature inside the actuator. An electric circuit, based on the voltage divider principle, was built to monitor the ink temperature as a function of the printing pattern. 'Dummy walls', located at the beginning and the end of the channel wall array, were used as temperature sensing elements. Since the dielectric permittivity of the PZT channel walls depends on temperature, the capacitance of the 'dummy walls' changes with temperature. The information obtained by this measurement technique was used to investigate alternative materials for the passive components of the actuator.

A further part was the development of a new actuator design called a 'Chevron actuator'. Chevron actuators include an additional PZT layer with polarization in the opposite direction to the base plate polarization. Thus, the whole channel wall is used as the active part instead of using just the upper half as in the standard actuator. The main advantage of this technique is a reduced power consumption of the actuator and therefore less heat dissipation.

Different approaches were used to construct Chevron actuators. Experiments determined the efficiency of the actuators and these results were used to make improvements. The Chevron actuators were characterized by the above mentioned techniques and compared with standard *Xaar* actuators.

ISBN 91-628-5675-8 • TRITA-FYS-5289 • ISSN 0280-316X • ISRN KTH/FYS/FTS/R--03/5289--SE

Preface

The present work in this thesis was carried out at the division of Condensed Matter Physics (KMF), Laboratory of Solid State Devices, in the Department of Microelectronics and Information Technology, Royal Institute of Technology (KTH), in Stockholm towards a Swedish Doctoral degree from October 1999 to June 2003 and was funded by *XaarJet AB* and by the Swedish agency *NUTEK*.

This thesis is divided into two parts. The first part, *Introduction*, gives a brief introduction into the field of inkjet printing. Different inkjet technologies are reviewed with main emphasize on *Xaar*-type shear mode actuators. Chapter 2 reviews the properties of lead zirconate titanate (PZT), the piezoelectric material Xaar actuators are made of. Chapter 3 describes the characterization techniques we have used.

The second part, *Our research*, describes and discusses experiments and new actuator designs in Chapters 4 to 6. Chapter 7 contains a summary of the included papers and manuscripts with comments on my participation.

This thesis is based on the following publications, manuscripts and patents

I. "Dielectric and Pulsed Spectroscopy of Shear Mode PZT Microactuator"
Jürgen Brünahl, Alex Grishin, and Sergey Khartsev
Mat. Res. Soc. Proc. **657**, EE4.6 (2000).

II. "Non destructive Pulsed Technique to Characterize Functional Properties of Micromachined Bulk PZT"
J. Brünahl, A.M. Grishin, and S.I. Khartsev
3rd Asian Meeting on Ferroelectrics, Hong Kong, December 2000
Ferroelectrics **263**, 187-192 (2001).

III. "Thermometry Inside Inkjet Actuators"
Werner Zapka, **Jürgen Brünahl**, Onne Wouters, and Mike de Roos
Proc. DPP 2001, International Conference on Digital Production Printing and Industrial Applications, 392-396, (2001).

IV. "Piezoelectric shear mode inkjet actuator"
Jürgen Brünahl, Alex M. Grishin, Sergey I. Khartsev, Carl Österberg
Mat. Res. Soc. Proc. **687**, B1.4 (2002).

V. "Piezoelectric shear mode drop-on-demand inkjet actuator"
Jürgen Brünahl, Alex M. Grishin
Sensors and Actuators A: Physical, Volume **101**, Issue 3, 371-382 (2002).

VI. ""Chevron"-type piezoelectric inkjet actuator"
Jürgen Brünahl, Alex M. Grishin
Proceedings of the 13th IEEE International Symposium on the Applications of Ferroelectrics, ISAF, 491-494 (2002).

VII. "Droplet Deposition Apparatus"
Werner Zapka, **Jürgen Brünahl**, Bosse Nilsson, and Mike de Roos
Xaar Technology Limited, WO Patent no. 02/26500, (2001).

VIII. "Fatigue of shear mode PZT actuator"
Vincent Ferrer, **Jürgen Brünahl**, Alex Grishin
Manuscript 2003.

The following papers have been published or submitted, but are not included in this thesis:

I. "Piezoelectric Chevron Inkjet Actuator by In-Process Polarisation Reversal"
Jürgen Brünahl, Gerald Richter, Thomas Jäger, Werner Zapka
Submitted to European Meeting on Ferroelectrics EMF 2003, Cambridge, UK.

II. "Depolarisation Damages of Lead Zirconate Titanate (PZT) Ceramics during Micromachining"
Jürgen Brünahl, Gerald Richter, Thomas Jäger, Werner Zapka
Submitted to European Meeting on Ferroelectrics EMF 2003, Cambridge, UK.

III. "Increased Inkjet Printing Frequency From 'Offset Channel' Printheads"
Werner Zapka, Mark Crankshaw, **Jürgen Brünahl**, Lars Levin, Uwe Hermann, and Götz Münchow
Submitted to NIP**19**: The l9th international Congress on Digital Printing Technologies 2003,New Orleans, USA.

Acknowledgements

First, I would like to thank my supervisors, Prof. Alex Grishin at *KTH* and Dr. Werner Zapka at *XaarJet AB*, for their professional guidance, constructive criticism, and not least for giving me the opportunity to study at the Department of Condensed Matter Physics.

I would also like to thank Dr. Sergey Khartsev for sharing his knowledge on ferroelectrics with me as well as for his generous technical assistance and many useful discussions.

Furthermore, I would like to thank *XaarJet AB* and all colleagues for making all the equipment available for my work and more important, I am grateful for having the possibility to work freely and independently with the appliances. My special thanks to Jan Eriksson and Mike de Roos.

I would like to thank all the people who joint me during the last years, Wolfgang Voit, my first roommate, my colleagues at KMF, Peter Johnsson, Sören Kahl, Mats Blomqvist, Vasyl Denysenkov, Jang-Yong Kim and Joo-Hyong Kim, and all the German students at Xaar, (even though unable to name all, I wish to thank Jorrit Rouwé, Gerrit Grunwald and Götz Münchow) for being such a nice company. Last but not least, I would like to thank Jung-Hyuk Koh and family for their generous hospitality during my Seoul visit.

Ett stort tack till mina kompisar, Eva, Åsa, Cissi, Staffan och Christer.

Finally, I want to thank Eva and Clara and my family for their constant encouragement and support.

Contents

Abstract iii

Preface iv

List of Papers v

I Introduction 3

1 Inkjet Technologies 5
1.1 History of inkjet technologies 5
1.2 Continuous inkjet 6
1.3 Drop-on-demand inkjet 7
1.3.1 Thermal inkjet 7
1.3.2 Piezoelectric inkjet 8
1.4 *Xaar*-type shear mode inkjet actuator 11
1.4.1 Design 11
1.4.2 Drop generation 12
1.4.3 Manufacturing 13
1.4.4 Print resolution 15
1.4.5 Geometrical aspects 16

2 Lead Zirconate Titanate (PZT) ceramics 23
2.1 History of PZT 23
2.2 Ferroelectricity and dipole structure 23
2.2.1 Ferroelectric domains 24
2.2.2 Polarization and poling 26
2.2.3 Ferroelectric hysteresis 26
2.2.4 Dielectric permittivity and dielectric loss 27
2.2.5 Electromechanical coupling coefficient 28
2.2.6 Curie temperature 28
2.3 Piezoelectricity 29

2.3.1 Definition of piezoelectric coefficients and directions 29
2.3.2 Piezoelectric effect 29
2.3.3 Lead zirconate titanate (PZT) 30
2.3.4 Shear mode displacement 30

3 Characterization techniques 33
3.1 Dielectric spectroscopy 33
3.2 Manual resonance test 35
3.2.1 Description 35
3.2.2 Behavior of PZT near mechanical resonance 36
3.3 Pulsed spectroscopy technique 38
3.4 Ferroelectric hysteresis *P*-*E* loop 40
3.5 Stroboscope technique 42
3.5.1 Drop velocity measurement 43
3.5.2 Drop volume measurement 43

II Our research 45

4 Physical properties of *Xaar* inkjet actuators 47
4.1 Temperature dependence of the dielectric properties 47
4.2 Frequency dispersion 48
4.3 Ferroelectric fatigue 50
4.4 Acoustic resonance modes 53
4.5 Correlation with inkjet performance 55

5 Thermometry inside inkjet actuators 57
5.1 Introduction 57
5.2 Theoretical background 58
5.2.1 Temperature compensation 58
5.2.2 Existing temperature compensation 58
5.2.3 Temperature dependence of channel wall capacitance 59
5.3 Experimental setup 61
5.3.1 Modification of the printhead 61
5.3.2 Electronics 61
5.4 Measurements 62
5.4.1 Calibration 62
5.4.2 Temperature differences induced by ink flow 63
5.4.3 Temperature differences induced by print pattern 63
5.5 Conclusions 67

6 Chevron-type inkjet actuator **69**
6.1 Introduction 69
6.2 Laminated Chevron design 71
6.2.1 Manufacturing 71
6.2.2 Optimization of active layer thicknesses 73
6.2.3 FEM simulations 76
6.2.4 Influence of glue joint thickness 77
6.2.5 Alternative bonding method 77
6.3 Monolithic Chevron design 78
6.3.1 Polarization set-up 78
6.3.2 Manufacturing 80
6.3.3 Functional performance 83
6.4 Conclusions 85

7 Summary of results **87**
7.1 "Dielectric and Pulsed Spectroscopy of Shear Mode PZT Microactuator" 87
7.2 "Non destructive Pulsed Technique to Characterize Functional Properties of Micromachined Bulk PZT" 87
7.3 "Thermometry Inside Inkjet Actuators" 88
7.4 "Piezoelectric shear mode inkjet actuator" 88
7.5 "Piezoelectric shear mode drop-on-demand inkjet actuator" 88
7.6 ""Chevron"-type piezoelectric inkjet actuator" 89
7.7 "Fatigue of shear mode PZT actuator" 89

Bibliography **89**

Index **93**

Papers I - VIII **93**

Appendix **93**

A PZT piezoelectric materials technical data **97**

To Eva and Clara

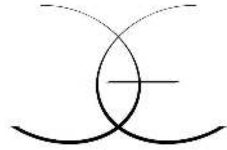

Part I

Introduction

Chapter 1

Inkjet Technologies

1.1 History of inkjet technologies

By 1878, Lord Rayleigh described the mechanism by which a liquid stream breaks up into droplets [1]. However, the first practical inkjet device based on this principle was patented in 1948 by *Siemens Elema* in Sweden [2]. In this invention a pressurized continuous ink stream was used to record the signal onto a passing recording media. In the early 1960s, R.G. Sweet from Stanford University demonstrated that by applying a pressure wave pattern, the ink stream could be broken into droplets of uniform size and spacing [3]. After break-off, electric charge could be impressed on the drops selectively. Whilst the charged droplets, when passed through an electric field, were deflected into a gutter for re-circulation, the remaining uncharged drops could fly directly onto the media to form an image. This printing process is known as *continuous inkjet*. In the 1970s, *IBM* launched a massive development programme to adapt continuous inkjet technology to their computer printers [4].

By the late 1970s, the first *Drop-on-Demand* inkjet methods appeared. A drop-on-demand device ejects ink droplets only when they are needed. Many of the drop-on-demand inkjet systems were invented, developed and produced commercially in the 1970s and 1980s, e.g. the *Siemens* PT-80 serial character printer [5]. In these printers, on the application of voltage pulses, ink drops are ejected by a pressure wave created by mechanical motions of piezoelectric ceramic actuators.

In 1979, *Canon* invented a method where ink drops were ejected from the nozzle by the growth and collapse of a water vapor bubble on the top surface of a small heater located near the nozzle [6]. *Canon* called this technology *Bubble-Jet*. Apparently at the same time, *Hewlett Packard* independently developed a similar inkjet technology and named it *ThinkJet* (thermal inkjet) [7]. It was the first successful low-cost inkjet printer based on the bubble jet principle.

Since the late 1980s, thermal inkjet or bubble jet printers have become a viable alternative to impact dot-matrix printers for home and office use. This is mainly because of their low cost, small size, quietness, and particularly their colour capability.

At present, two classes of inkjet technologies are available: continuous jet and drop-on-demand. The most common designs of printers based on these technologies are shown in Fig. 1.1 to Fig. 1.6 and will be discussed briefly below. Additional information on inkjet printing can be found in Ref. [8, 9, 10, 11].

1.2 Continuous inkjet

Continuous inkjet technology permits very high-rate drop generation, one million drops per second or faster, but is expensive to manufacture and to operate. Two classes of continuous inkjet printers are available today. High-speed industrial printers are used for applications such as carton and product marking and addressing and personalizing direct mail. Proofing printers on the other hand offer the best print quality among non-photographic devices, but they are much slower. Although the resolutions are not that high (e.g. 300 dpi), the variable-sized dots make photographic quality possible.

A simplified sketch of a typical continuous jet printing system is shown in Fig. 1.1. Ink under pressure is delivered from an ink reservoir via an input line to a head structure. The head structure, containing a piezoelectric driver plate, is periodically constricted at it's mechanical resonance frequency by means of an applied electric field . By this method, an ink stream discharged from it breaks up into a plurality of individual drops. A charging electrode applies charge to each of the drops. The magnitude of the charge placed on individual drops is variable and determines the drops' ultimate paths. After the drops have exited the charging electrode, they pass between a pair of deflection plates, to which a fixed potential is applied. Drops that are utilized for printing are deflected to a media to form

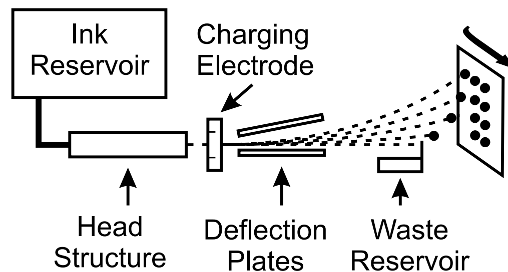

Figure 1.1. Functional principle of a continuous inkjet system

characters while excess drops are directed to a gutter, which in turn directs the drops to a waste reservoir [12].

1.3 Drop-on-demand inkjet

For drop-on-demand systems, which are microelectromechanical systems (MEMS) that deliver droplets only when needed, several methods of actuating are proposed. Most common is thermoelectric actuation followed by the piezoelectrically driven actuators. Especially the piezoelectric inkjet technology with its ability to print a variety of fluids is developing in many different directions. Besides printing ink on paper, new applications can be found in very specific fields such as e.g. biochemistry (DNA printing) or printing of organic polymers, solid particles or adhesives [13, 14, 15].

The two most common technologies are thermal inkjet (used by e.g. *Hewlett Packard* and *Canon*) and piezoelectric inkjet (used by e.g. *Xaar*, *Epson* and *Brother*).

1.3.1 Thermal inkjet

The operating sequence of a thermal inkjet system (Fig. 1.2) starts with a current pulse passing through a resistive layer (heater) in the ink filled channel. The resistive layer is located near the orifice or nozzle for that channel. Heat is transferred from the resistor to the ink. The water-based ink becomes superheated (far above its normal boiling point) and finally reaches the critical temperature for bubble nucleation of around 280 °C. Once nucleated, the bubble or water vapour thermally isolates the ink from the heater and no further heat can be applied to the ink. The bubble expands until all the heat stored in the ink in excess of the normal boiling point is used to convert liquid to vapour. The expansion of the bubble forces a droplet of ink out of the nozzle. Once the excess heat is removed, the bubble collapses on the resistor. The resistor at that point is no longer being heated because the current pulse has passed and the droplet is propelled at high speed in the direction of a recording medium. The ink channel refills by capillary action. The entire bubble formation and collapse sequence occurs in about 10 µs. The channel

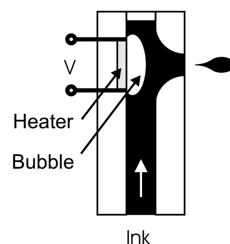

Figure 1.2. Principle of a thermal inkjet system (also known as Bubble-Jet)

can be refired after a 100 to 500 µs minimum dwell time to enable the channel to be refilled [16].

1.3.2 Piezoelectric inkjet

Piezoelectric inkjet printers harness the inverse piezoelectric effect, which causes certain crystalline materials to change shape when a voltage is applied across them. A small electrical pulse makes the crystal contract slightly, squeezing ink out of the nozzle onto the media.

Depending on the piezoelectric ceramics' deformation mode, the technology can be classified into four main types: squeeze, bend, push, and shear. For squeeze mode, radially polarized ceramic tubes are used. In both, bend- and push-mode design, the electric field is generated between the electrodes parallel to the polarization of the piezomaterial. In a shear mode printhead, the electric field is designed to be perpendicular to the polarization of the piezoceramics.

Squeeze mode actuator

The actuator of a printhead working in a squeeze mode, as displayed in Fig. 1.3, comprises piezoelectric ceramic tubing with a diameter of about 1 mm. The tube, which is polarized radially, is provided with electrodes on its inner and outer surface. When it is desired to have a droplet expelled from the orifice, a short rise time voltage pulse is applied to the transducer, the polarity being selected to cause a contraction of the transducer. The resulting sudden decrease in the enclosed volume causes a small amount of liquid to be expelled from the orifice. Due to the pressure pulse, some of the ink is also forced back into the tube, but the amount is relatively small due to the high acoustic impedance created by the length and small bore of the tube. The voltage pulse is allowed to decay relatively slowly and the transducer, therefore, expands slowly to its initial volume. Due to the small rate of change of volume during the decay, the accompanying pressure reduction is too small to overcome the surface tension at the orifice. Consequently, liquid flows into the transducer to replace the liquid previously expelled without drawing in air through the orifice. This printhead design was implemented, e.g., in the *Siemens PT-80* printer.

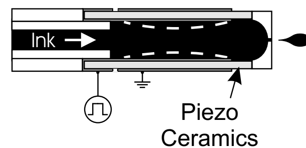

Figure 1.3. Squeeze mode actuator design

Bend mode actuator

Fig. 1.4 shows a piezoelectric inkjet printhead operating in bend mode. It consists of a pressure chamber including an ink inlet and an outlet passage terminated in an orifice. A conductive diaphragm forms one side of the chamber with a deflection plate made of piezoelectric ceramic attached. The outer surface of the plate is covered by a conductive coating, which provides an electrical connection to the plate. Applying a voltage to the piezoelectric plate results in a contraction of the plate thereby causing the diaphragm to flex inwardly into the pressure chamber. This, of course, applies pressure to the printing fluid in the chamber, which forces a droplet to be expelled from the orifice. The size of the droplets is defined by the voltage applied to the deflection plate, the pulse duration, and the diameter of the orifice [17]. The printheads in *Tektronix*'s *Phaser* and *Epson*'s *Color Stylus* inkjet printers are based on this design principle.

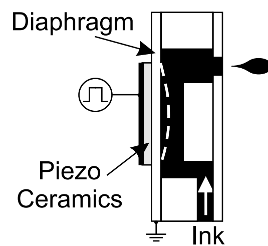

Figure 1.4. Principle of the bend mode technique

Push mode actuator

In a push mode design (Fig. 1.5), as the piezoelectric ceramic rod expands, it pushes against a diaphragm to eject the droplets from an orifice.

In theory, the piezoelectric actuators can directly contact and push against the ink. However, in practical implementation, a thin diaphragm between the piezoelectric actuators and the ink is incorporated to prevent the undesirable interaction between ink and actuator materials [18]. Successful implementation of the push mode piezoelectric inkjet is found in printheads from companies such as *DataProducts*, *Trident*, and *Epson*.

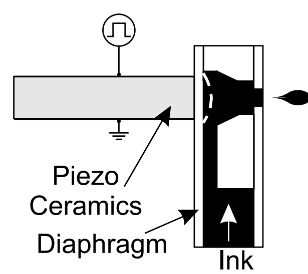

Figure 1.5. Functional principle of a push mode inkjet actuator

1.4 *Xaar*-type shear mode inkjet actuator

This chapter describes the design and the functionality of piezoelectric *Xaar*-type shear mode inkjet actuators (herein after referred to as '*actuator*').

1.4.1 Design

In the Swedish Xaar facility printheads with 64, 128 and 500 channels are produced, and each version can print at a resolution of 200 dpi (*dots per inch*) and 360 dpi.

The actuator is composed of a base plate made of poled piezoelectric lead zirconate titanate (PZT) ceramic , and an inactive cover plate made of unpoled PZT. Figs. 1.6 show an exploded view of the components of an actuator (a) and of an assembled actuator (b). The base plate contains a multitude of ink channels . In the exploded view, the bottom of an ink channel is clearly seen. The channels have a shallow bottom near the bond pad and become deeper in the main part. Metal

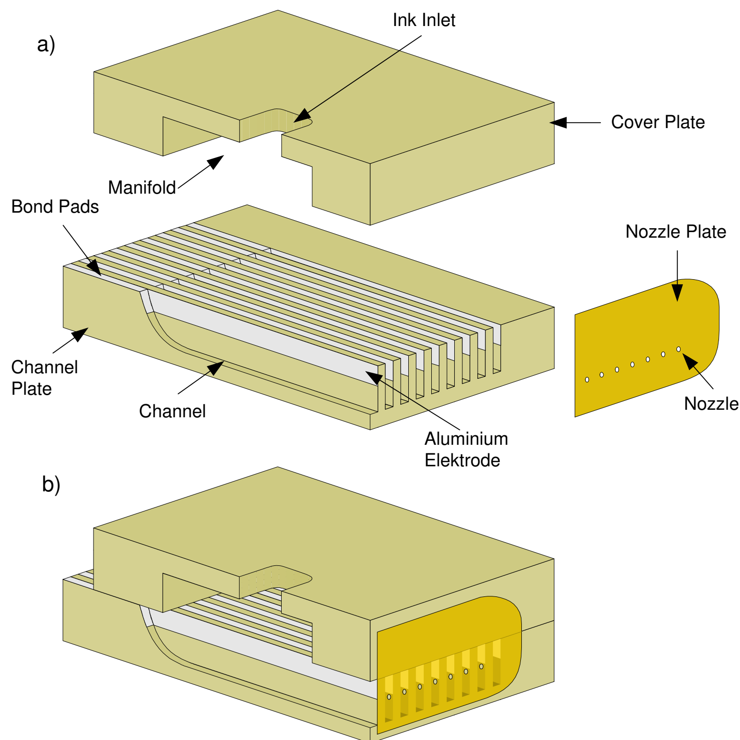

Figure 1.6. Exploded view of a *Xaar*-type actuator showing a) components and b) an assembled actuator

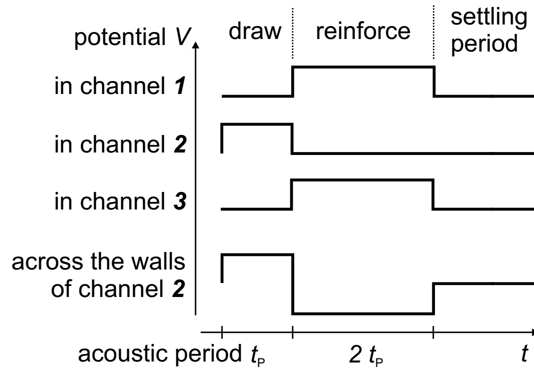

Figure 1.7. Typical waveforms of the driving voltage signal applied to the shear mode actuator for drop generation.

electrodes are deposited on the upper half of both sides of the channel wall. The electrodes within one channel are connected galvanically at the wire bond area. The cover plate is glued onto the base plate. It forms the roof of the ink channels, and clamps the top of the channel wall rigidly (Fig. 1.6b). A nozzle plate is assembled onto the actuator front surface. Ink is fed into the channels through an ink inlet in the cover plate [19, 20].

1.4.2 Drop generation

For drop generation, driving voltage signals (Fig. 1.7) are applied to the electrodes, generating fields perpendicular to the direction of polarization in the channel walls. This produces shear mode displacement in the upper half of the channel wall. The lower halves of the channel walls are forced to follow the motion of the upper halves, so the channel walls deform into approximate chevron shapes as shown in Fig. 1.8 and Fig. 1.13. Appropriate temporal voltage waveforms with opposite polarity

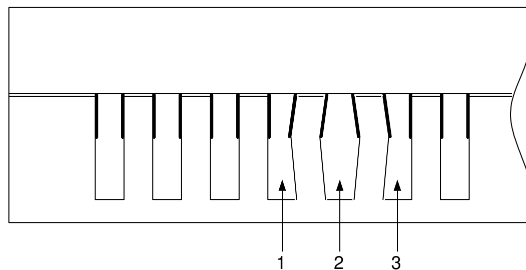

Figure 1.8. Cross section of a *Xaar*-type actuator showing wall displacement due to applied electric fields.

to both walls of an ink channel, say channel number '2' in Fig. 1.8, will cause fast transient increase and decrease of the channel volume. Acoustic compression waves move inwards from the manifold and nozzle ends of the channel, restoring atmospheric pressure as they advance and inducing flow into the channel from the manifold and from the meniscus at the nozzle. The waves cross in the middle, producing a region of pressure above atmospheric in the center of the channel. After one acoustic period (t_p) - the time for a wave to travel the length of the channel - there is an elevated pressure all along the active channel.

At this moment a step in the waveform applied to the channel '2' and an opposite step in the waveform applied to its neighbours cause the walls to move inwards, and further pressure is created in the channel. Now acoustic rarefaction waves travel along the channel, reducing the pressure back to atmospheric, and there is flow out of the channel into the manifold and into the nozzle. Thus a drop is ejected over the acoustic period.

The waveforms return to ground, typically, one acoustic period later. This cancels most of the acoustic waves, which remain in the channel. There is a variable settling period before further waveforms are applied.

1.4.3 Manufacturing

Manufacturing of shear mode printheads involves various processes, which are critical to get high yield and performance of the actuators. The first is the machining of PZT ceramics . It is not possible to use parallel processes, therefore the channels are sawn serially using a semiconductor-industry dicing saw. The advantage of using a numerically controlled process is that alternations can be programmed easily. It is also possible to make long arrays of channels. Special cooling arrangements are needed to prevent PZT depoling under local heating and stress. Care is taken to minimize grain pullout, as this leads to reduction in the effective piezoelectric thickness of the channel walls.

Metallic electrodes are prepared by a physical vapor deposition process in vacuum. A crucible of molten aluminium is heated by a scanned electron beam, and evaporates atoms in a direction broadly towards the actuators. The channelled PZT component is tilted, first one way and then the other, so that each channel wall shadows its neighbour and limits the depth of plating to the top half of the channel (see Fig. 1.9). Argon ion bombardment is used to clean channel wall surfaces before the deposition of aluminium, and is continued during the first stage of metallization to ensure good adhesion by driving the aluminium atoms into the PZT structure.

The metallization needs to be patterned to galvanically disconnect electrodes on the opposite sides of the channel walls and to produce wire bond pads. This is done photolithographically: prior to metallization, a resist is applied everywhere, masked and exposed with UV light in the places where aluminium will not be required; the unexposed resist is washed off, and then the metallization is carried out. Then a lift-off removes the exposed resist and aluminium where plating is not wanted.

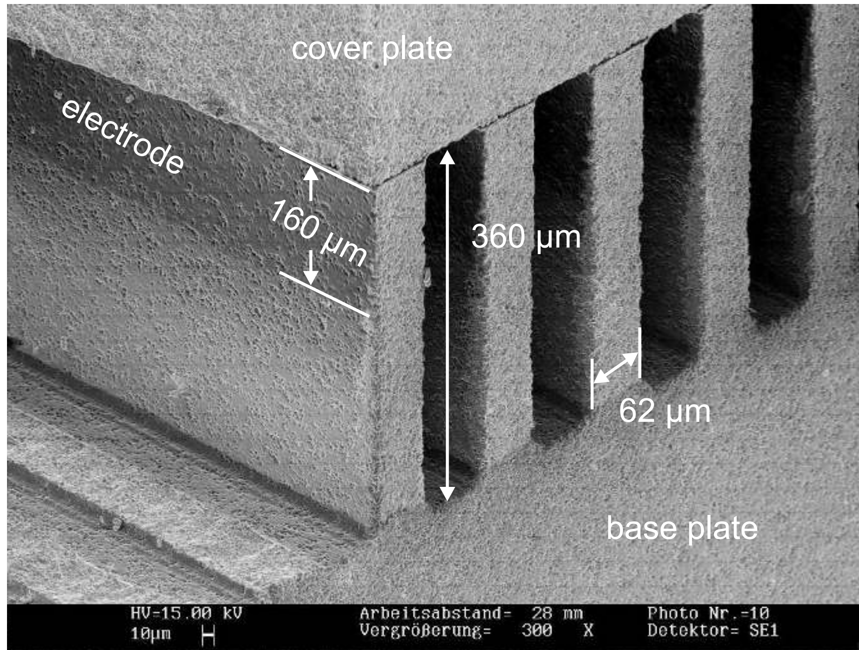

Figure 1.9. SEM micrograph (×300) of a ferroelectric PZT ceramics with an array of micromachined actuating elements and its dimensions. Each single channel wall is plated from both sides with aluminium electrodes.

After metallization silicon nitride passivation is applied. The passivation is intended as an ion and electron barrier, to prevent corrosion of the electrodes by ink. The whole surface of the channelled base plate, except wire bond areas, is coated with silicon nitride by electron cyclotron resonance chemical vapor deposition, using plasma of silane, nitrogen and argon. The cyclotron radiation excites the plasma in such a way as to produce deposition of silicon nitride with very low inclusion of hydrogen and without producing excessive heating - the Curie temperature of the PZT must not be exceeded.

Next the cover is glued to the channelled component. The necessary thin, rigid bond is achieved by the use of a press. It is essential that both PZT components and one of the platens of the press are highly flat, and that the other platen has the correct degree of compliance. The adhesive has to be extremely well mixed, because inhomogeneities on the micrometer scale of the bond line thickness lead to variations in the stiffness of channel walls.

All the processes described so far are carried out at wafer scale. At this stage, the single actuators are diced apart, guaranteeing the coplanarity of the two components at the nozzle plate face. The polyimide nozzle plates are attached with a thin layer of adhesive [21].

1.4.4 Print resolution

Resolution is the basic term used to classify printers and is most commonly expressed by the unit *dots per inch* (dpi). It denotes the number of clearly resolved points a printhead theoretically can print in a one-inch interval. If two numbers are given, the first number indicates the horizontal resolution and the second number the vertical resolution, e.g. 1440×720 dpi for an *Epson Stylus Color* 860 printer. [22]

Typical values of a Xaar XJ128-360dpi printhead are shown in Table 1.1 [23].

Table 1.1. XJ128-360 specifications

Property	Typical value
Resolution, dpi	360
Firing frequency, kHz	8.3
Linear speed, m/s	0.59
Number of channels	128
Print width, mm	8.9

The horizontal resolution when head/paper movement is horizontal is defined by the firing frequency of the printhead and the linear speed of its horizontal movement. E.g., firing the printhead at its maximum firing frequency of 8.3 kHz with a linear speed of 0.59 m/s results in a horizontal distance between impinging drops of approximately 70 µm, which corresponds to a resolution of 360 dpi. To achieve the vertical resolution it is necessary to know the number of channels and the print width. E.g., 128 channels at a print width of 8.9 mm will result in a vertical drop distance of approximately 70 µm, which corresponds to a resolution of 360 dpi. The vertical resolution of a printer depends also on the positioning accuracy of the mechanical paper feed. Since firing frequency and linear speed can be controlled much better than the positioning accuracy of the paper feed, a printers horizontal resolution can be much higher than the vertical resolution.

Three additional parameters are important to maintain the resolution of a printhead: drop volume, drop velocity and angular deviation from the center line of drop ejection. The volume of a drop should be sufficient to cover the area defined by the resolution. E.g., if the resolution is 360 dpi, the area to be covered by one drop is $70 \times 70\ \mu m^2$. Since the drop area is circular the dot diameter has to be exactly the same value as the diagonal of the area defined by the resolution (for the example 99 µm). The intersection should be as little as possible as shown in Fig. 1.10a. If the volume is too small, the printout looks pale because uncovered parts of the media are still visible (Fig. 1.10b). If the volume is too big, neighboring spots will merge and the printout looks blurred (Fig. 1.10c). The drop volume is predefined by channel volume and nozzle diameter and depends also on properties of the piezoelectric ceramics. Stronger displacement of the wall results in higher drop volume.

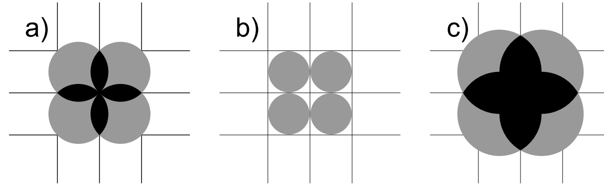

Figure 1.10. Effect of the drop size on paper coverage. a) optimal coverage; b) drops too small; c) drops too big.

Fluctuations of drop velocity strongly influence the horizontal resolution of a printer. If firing frequency and linear movement of the printhead are constant, then any difference in drop velocity will change the distance between two neighboring dots on the media. E.g., assuming a drop velocity of 7 m/s and 1 mm distance between nozzle and media, the time for a droplet to reach the media is 1/7000 s. At the same time a printhead with a linear speed of 0.59 m/s moves a distance of 84 µm. If the drop velocity decreases by 10%, the distance moved by the printhead is 10% lager which is already 12% of dot distance at 360 dpi resolution. Drop velocity depends very much on properties of the PZT ceramics such as piezoelectric charge constant d_{15}, magnitude, and direction of the polarization.

Angular deviations from the drop ejection center line cause similar problems as differences in drop velocity. Depending on the degree and the direction of the angular deviation both horizontal and vertical resolution can be affected. A deviation of 1 degree misplaces a dot by 22 µm, if the distance between the nozzle and media is 1 mm. These deviations can occur, e.g., if the shape of the nozzle is not optimal or if particles are clogging parts of the channel or nozzle, but they do not depend on the properties of PZT ceramics.

1.4.5 Geometrical aspects

The following considerations on pressure in the channel, effect of wall thickness and nozzle size are derived by Rolf Kaack and described in his master's thesis [24] produced at *XaarJet AB* in July 2001.

Pressure in the channel

The fluid characteristics of the actuator can be derived from the continuity equation

$$-\oint j dA = \frac{dm}{dt} \tag{1.1}$$

The left side of the equation describes the mass flow density j flowing into or out off the surface A of a given system, here the openings of a channel, while the right

side can be seen as another expression for the change in the channel volume due to the wall movement. When applying Eq. 1.1 to the given case, it follows that

$$-\Phi = \frac{dV_{wall}(p,U)}{dt} \tag{1.2}$$

with Φ the total flow into or out of the channel. The function $V_{wall}(p,U)$ describes the coupling between the volume displacement of the wall, the voltage U, that is applied to the wall, and the pressure p, caused by the ink in the channel. The time dependency of the pressure can be evaluated from equation 1.2

$$\frac{dp}{dt} = -\frac{\Phi + \left.\frac{dV_{wall}}{dU}\right|_p \frac{dU}{dt}}{\left.\frac{dV_{wall}}{dp}\right|_U}. \tag{1.3}$$

The flow Φ could be seen as the product of the drop velocity times the surface, through which the ink is ejected.

$$\Phi = v_{nozzle}(p) \cdot A_{nozzle}(p) + v_{rear}(p) \cdot A_{rear} \tag{1.4}$$

It is insightful, that the drop speed is a function of the pressure. The actual ink jet diameter, $A_{nozzle}(p)$, is of a smaller diameter than that of the nozzle cross section. The reason is that the surface tension between ink and nozzle restricts the effective nozzle outlet. Also the non-wetting coating of the nozzle plate probably has an influence.

The drop ejection is a very dynamic process, and a lot of parameters must be taken into account, which may not always be of linear character. Thus Eq. 1.3 may only be solved numerically.

Effect of the wall thickness

Drop volume

The voltage applied to the wall leads to an electric field across the wall, which, in turn, causes a wall deflection due to the piezoelectric effect. The deflection can be described as

$$\tan\alpha = \frac{y(x)}{x} = d_{15} \cdot \frac{U}{b} \tag{1.5}$$

where d_{15} is the piezoelectric coefficient for the shear mode, b, $y(x)$ and α are as shown in Fig. 1.11. The resulting volume displacement V can be calculated easily when assuming a simple movement of stiff walls as shown in the prementioned figure. V is then

$$V = 2z \int_0^{h/2} y(x)\,dx = \frac{d_{15} z h^2}{4b} \cdot U \tag{1.6}$$

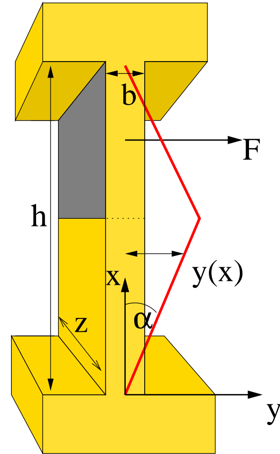

Figure 1.11. Cross section of the wall

Assuming incompressibility of the ink, the ejected ink amount must be as big as the volume displacement V. Since the ink is ejected through both channel outlets at the nozzle and at the manifold, the volume of the ejected drop, which is equal to the volume that is ejected through the nozzle, depends on the fluidic resistances R_{nozzle} and R_{rear} of both openings of the channel. As the walls of a firing channel first bend outwards and then inwards, the total V_{nozzle} must be multiplied by 2.

$$V_{nozzle} = 2\,\frac{R_{rear}}{R_{nozzle} + R_{rear}} \cdot V \tag{1.7}$$

The fluidic resistances are difficult to describe. At the rear end the pressure of the ink in the manifold must also be taken in account.

The effect of the pressure of the ink in the channel has not been taken in account in the calculation above, because the pulse lengths of the signals, that are applied to the printhead, are long enough to give the pressure the possibility to equalize or even to become negative. Thus it can be assumed, that the total volume displacement, that can be reached, corresponds to V_{nozzle} as calculated in Eq. 1.7.

Drop velocity

It can be assumed that the drop velocity is strongly affected by the pressure in the channel, which in turn depends on the wall width. A reduced wall width leads to a higher electric field being applied across the wall, which results in a higher pressure in the channel. But the reduced wall width also leads to a lower rigidity of the walls, diminishing the pressure in the channel.

Furthermore, the surface of the rear end of the channel, A_{rear} in Eq. 1.4, increases with a thinner wall. Thus it could be, that the effects of the wall width b in the different terms in Eq. 1.3 canceled each other more or less, so that the effect of a thinner wall on drop velocity seems to be quite small.

Effect of the nozzle diameter

Referring to Eq. 1.4, the flow through the nozzle is a function of the surface $A_{nozzle}(p)$. It can be seen as the effective surface through which the ink jet is ejected. As described above, it does not only depend on the pressure, but is also a function of the meniscus force and the surface tensions between ink and nozzle. A bigger nozzle diameter leads to a smaller meniscus force and a smaller influence of the surface tensions, that, in turn, lead to a higher $A_{nozzle}(p)$.

Finite element method (FEM) simulation

To get an idea of the real shape of the deformed channel wall Finite Element Method (FEM) analysis using ANSYS software was performed.

Fig. 1.12 depicts the movement of a non-clamped actuator wall with a height of 385 µm due to an applied voltage of 22 V, which is the typical driving voltage. Electrode coverage was 43% from the top of the wall.

The shear motion has two components [25], which are also clearly visible in the FEM. The non-clamped wall has its maximum lateral displacement of 14.2 nm at the top of the wall.

Clamping the wall on the top leads to a change in the shape of the deformation. Both shear motions merge to a single chevron shaped displacement of the wall as displayed in Fig. 1.13. The maximum deformation of 26.6 nm is now at the point were the electrode ends, approximately 43% from the top. So, clamping the wall at the top doubles the displacement.

Performing resonance analysis on the channel wall model given in Fig. 1.13 gave resonance frequencies which where about 16% higher than measured values (for details see Chapter 4). The simplified structure of the model was identified as the reason. For better results the model was improved by adding the following components (depicted in Fig.1.14):

- additional PZT bulk material at top and bottom of the channel wall;
- glue layer between cover plate and channelled component;
- curvature at the bottom of the channel wall;
- aluminium (Al) electrodes;
- Silicon nitride (SiN) passivation;

Using these improvements it was possible to refine the resonance behavior to meet real measurements. Table 1.2 shows the percentage affect on the simulated resonance of the channel wall.

From Table 1.2 we see that including additional PZT bulk material at top and bottom of the channel wall yields values close to real measured data. All other modifications change the resonance frequency marginally. Therefore, only

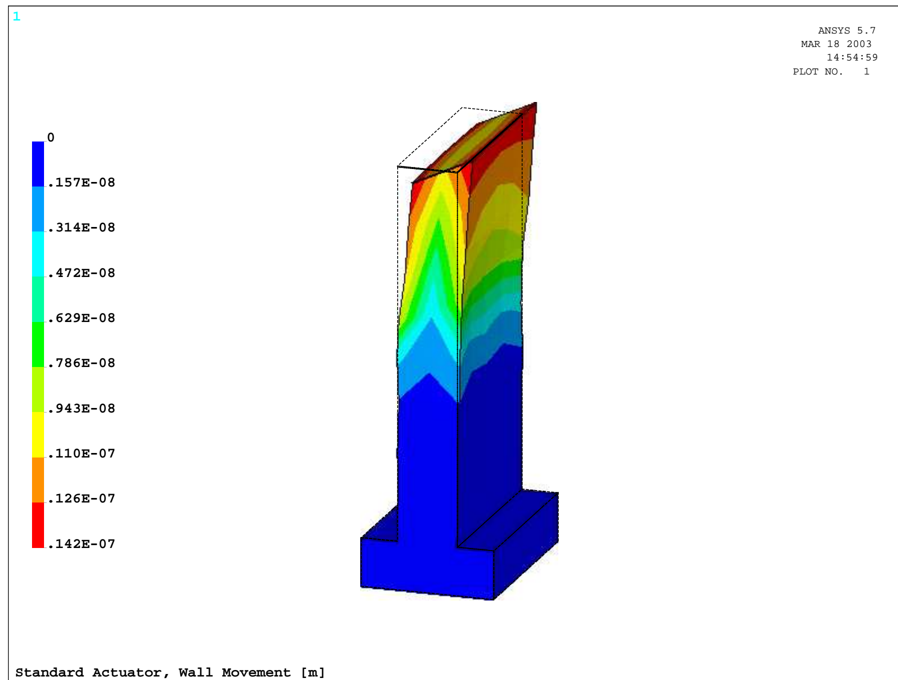

Figure 1.12. FEM analysis showing wall movement of a non-clamped channel wall

the model with the additional bulk PZT was used for further simulations to keep the computing time as short as possible.

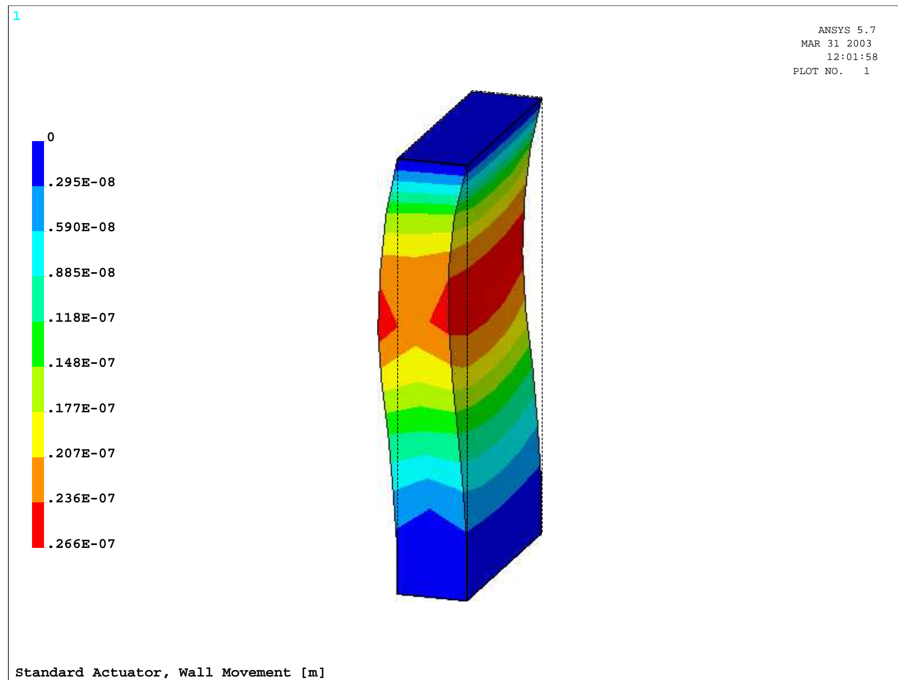

Figure 1.13. FEM analysis showing wall movement of a standard **Xaar** actuator

Table 1.2. Influence of wall components to the resonance behavior of a XJ128-200 actuator.

Model	resonance frequency, MHz	deviation in percent
simplified **w**all (SW)	1.070	+16
SW + Al + SiN	1.100	+20
SW + bulk on top and bottom	0.925	+1
SW + bulk on top and bottom + glue layer	0.883	-4
SW + bulk on top and bottom + glue layer + curvature	0.895	-3
SW + bulk on top and bottom + glue layer + curvature + Al + SiN	0.915	-1

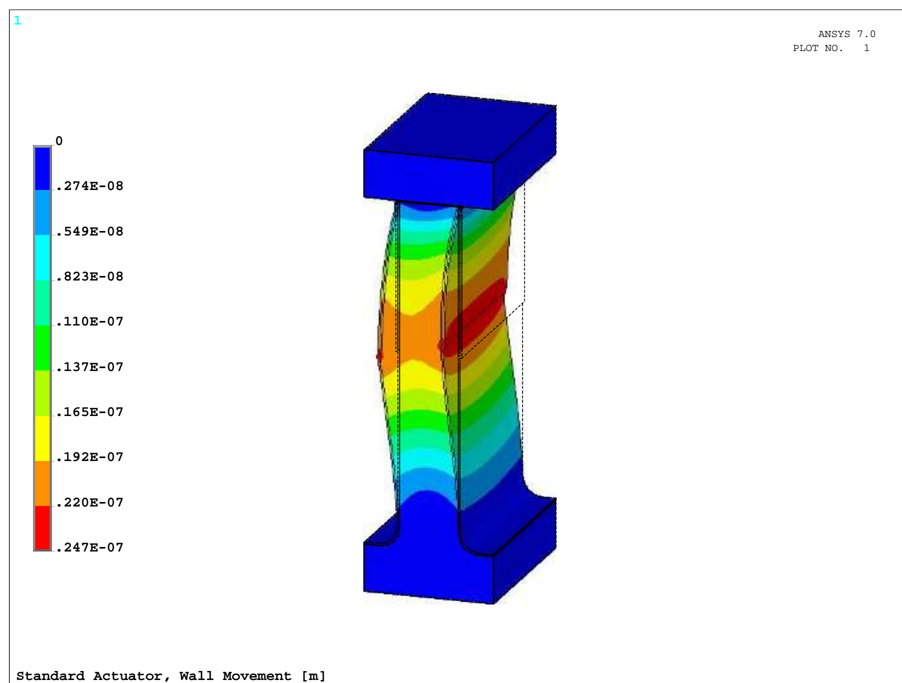

Figure 1.14. FEM analysis showing wall movement of the improved model of a standard **Xaar** actuator.

Chapter 2

Lead Zirconate Titanate (PZT) ceramics

2.1 History of PZT

The piezoelectric effect (electricity from applied stress) was first discovered by Pierre and Jacques Curie in 1880. Their experimental demonstration consisted of a conclusive measurement of surface charges appearing on specially prepared crystals, which were subjected to mechanical stress. In 1881, Gabriel Lippmann deduced mathematically the inverse piezoelectric effect (stress in response to applied electric field). The Curie brothers immediately confirmed the existence of this property. In the following years the 20 natural crystal classes in which piezoelectric effects occur and all 18 possible macroscopic piezoelectric coefficients were defined. [26]

Barium titanate ($BaTiO_3$), the first piezoelectric ceramic with perovskite structure, was found around 1943. S. Roberts detected the piezoelectric effect in $BaTiO_3$ in 1947. In 1954, the discovery of the piezoelectric ceramic lead zirconate titanate $Pb(Zr_xTi_{1-x})O_3$ (PZT) was reported by B. Jaffe *et al.*. In the following years PZT became the main industrial product in piezoelectric ceramic materials.

Recently, piezoelectric materials in thin film form attracts much attention as a key element for high-frequency surface and bulk acoustic wave devices and micro electromechanical systems (MEMS).

2.2 Ferroelectricity and dipole structure

Ceramic perovskites have a cubic (fcc+bcc) structure that is stable at temperatures above their Curie temperature (T_c) as seen in Fig. 2.1a. When the temperature decreases and falls below T_c the structure changes and in the case of PZT, the O^{2-} and the Pb^{2+} -ions are moved from their cubic positions and the Ti^{4+} and Zr^{4+}

ions are moved from the center of the cube (Fig. 2.1b). This results in a dipole and a structure that is no longer cubic but rather tetragonal.

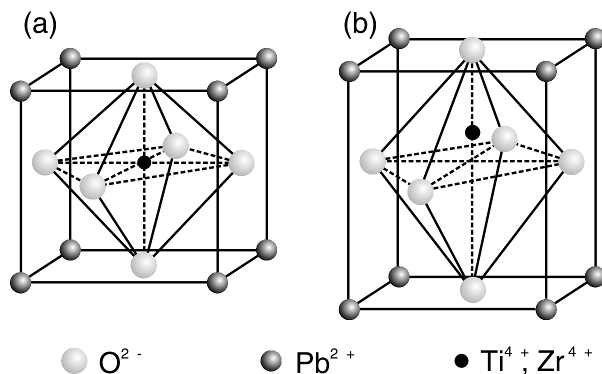

Figure 2.1. a) Cubic ($T \geq T_c$) and b) tetragonal ($T < T_c$) structure of the PZT unit cell

2.2.1 Ferroelectric domains

In general a uniform alignment of the electric dipoles only occurs in a certain regions of a crystal, while in other regions the polarization may be in the reverse direction. Such regions are called ferroelectric domains. Fig. 2.2a shows a schematic drawing of the atomic displacement on both sides of the domain boundary. Fig. 2.2b and the SEM micrograph in Fig. 2.3 show typical domain structures.

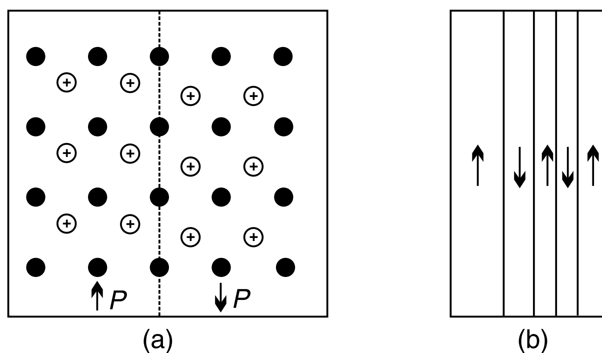

Figure 2.2. a) atomic displacement at the domain boundary; b) domains in a ferroelectric material

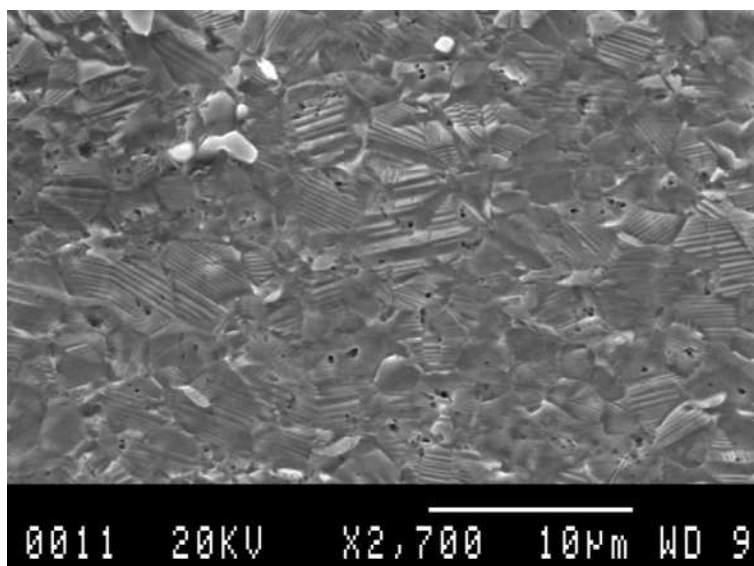

Figure 2.3. SEM micrograph showing domain structure of PZT ceramic

2.2.2 Polarization and poling

When a ferroelectric ceramic is produced, it shows no piezoelectricity. Because of the random orientation of the different grains and the existence of the domains, there is no net polarization. In order for the material to become piezoelectric it has to be poled.

Poling is the imposition of a DC-voltage across the material. The ferroelectric domains align to the field resulting in a net piezoelectric effect. Not all the domains become exactly aligned. Some of them align only partially and some do not align at all. The number of domains that do align depends upon the electric poling field, the temperature and the time the electric field is held on the material. During poling the material permanently increases in dimension between the poling electrodes (Fig. 2.4). The material can be depoled by reversing the poling voltage, increasing the temperature beyond the Curie temperature or by inducing a large mechanical stress. [27]

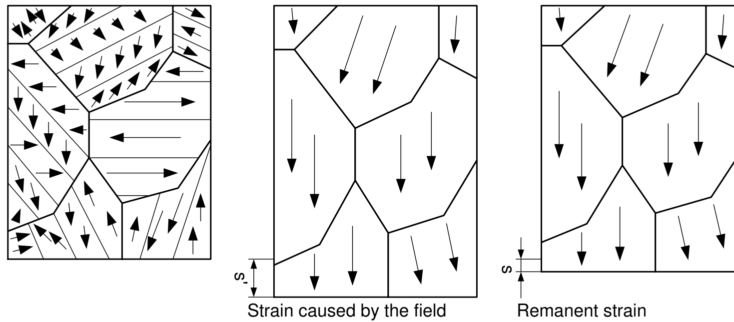

Figure 2.4. Schematic drawing of the poling process for piezoceramics

2.2.3 Ferroelectric hysteresis

A ferroelectric hysteresis loop for a piezoelectric ceramic is a plot of the polarization P developed against the field E applied to that device at a given frequency. A typical hysteresis loop is shown in Fig. 2.5. Applying a small electric field, we only get the linear relationship between P and E (1→2), because the field is not large enough to switch any domain and the sample will behave as a normal dielectric material. As the electric field strength increases (2→3), a number of the negative domains (which have a polarization opposite to the direction of the field) will be switched over in the positive direction and the polarization will increase rapidly until all domains are aligned in the positive direction (4). As the field strength decreases, the polarization will generally decrease but not return back to zero. When the field is reduced to zero (5), some of the domains will remain aligned in the positive direction and the ferroelectric sample will exhibit a *remnant polarization* P_r. [28]

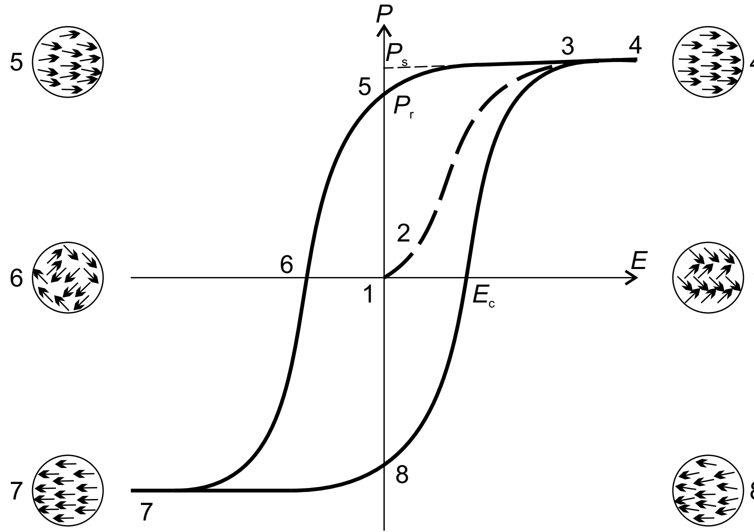

Figure 2.5. P-E hysteresis loop parameters for a ferroelectric material

The remnant polarization P_r in a ferroelectric sample cannot be removed until the applied field in the opposite (negative) direction reaches a certain value. The strength of the field required to reduce the polarization P to zero (6) is called the *coercive field strength* E_c. Further increasing of the field in the negative direction will cause a complete alignment of the dipoles in this direction (7). Reversing the field direction once again can complete the hysteresis cycle.

2.2.4 Dielectric permittivity and dielectric loss

The dielectric permittivity ε_r can be interpreted as the relative amount of storable charges in equivalent geometric capacitors.

For most applications of ferroelectric materials, the dielectric permittivity and dielectric loss are important practical parameters. Suppose a parallel capacitor is filled with a dielectric medium. When an alternating electromotive force F with frequency ω is applied on this capacitor, an alternating current i flows through the capacitor,

$$i = j\omega\varepsilon_r C_0 F \qquad (j = \sqrt{-1}) \tag{2.1}$$

where C_0 is the capacity of the parallel plate capacitor without any medium (i.e. in vacuum) and ε_r, the relative dielectric constant, is a function of ω. Because dielectric loss (including leakage current) exists in dielectric materials, ε_r must be written as a complex number:

$$\varepsilon^*(\omega) = \varepsilon'(\omega) - j\varepsilon''(\omega), \tag{2.2}$$

where $\varepsilon'(\omega)$ is the real part of the dielectric constant and $\varepsilon''(\omega)$ is the imaginary part. The later represents the dielectric loss. Instead of ε'', $tan\delta$ (tangent of the dielectric loss angle) is most frequently used and can be expressed by:

$$tan\delta = \frac{\varepsilon''}{\varepsilon'} \tag{2.3}$$

2.2.5 Electromechanical coupling coefficient

Electromechanical coupling coefficients k_{33}, k_{31}, k_p, and k_{15} describe the conversion of energy by the ceramic element from electrical to mechanical form or vice versa. The ratio of the stored converted energy of one kind (mechanical or electrical) to the input energy of the second kind (electrical or mechanical) is defined as the square of the coupling coefficient.

$$k = \sqrt{\frac{\text{mechanical energy stored}}{\text{electrical energy applied}}} \quad \text{or} \quad k = \sqrt{\frac{\text{electrical energy stored}}{\text{mechanical energy applied}}} \tag{2.4}$$

Subscripts denote the relative directions of electrical and mechanical quantities and the kind of motion involved. They can be associated with vibratory modes of certain simple transducer shapes; k_{33} is appropriate for a long thin bar, with electrodes on the ends, polarized along the length, and vibrating in a simple length expansion and contraction. k_{31} relates to a long thin bar, with electrodes on a pair of long faces, polarized through thickness, and vibrating in simple length expansion and contraction. k_p signifies the coupling of electrical and mechanical energy in a thin round disc, polarized through thickness and vibrating in radial expansion and contraction. k_{15} describes the energy conversion in a thickness shear vibration. Since these coefficients are energy ratios, they are dimensionless. [29]

2.2.6 Curie temperature

An important parameter of ferroelectrics is the temperature of phase transition , called the Curie temperature T_c. When temperature decreases through the Curie temperature, a ferroelectric crystal undergoes a structural phase transition from a paraelectric phase to a ferroelectric phase. In most ferroelectrics, the temperature dependence of the dielectric constant can be described by the Curie-Weiss law:

$$\varepsilon' = \varepsilon_0 \left(1 + \frac{W}{T_c - T}\right) \tag{2.5}$$

where W is the Curie-Weiss constant and T is the temperature.

Usually, the temperature independent term ε_0 can be neglected, because it is much smaller than the term $\varepsilon W/(T - T_c)$ when T is near T_c.

2.3 Piezoelectricity

2.3.1 Definition of piezoelectric coefficients and directions

To identify directions in a piezoelectric ceramic element, three orthogonal axes are used, termed 1, 2 and 3 (Fig. 2.6). The polar, or 3 axis, is always taken parallel to the direction of polarization within the ceramic. The indexes 4, 5 and 6 represent a shear movement around the 1, 2 and 3 axis. To link electrical and mechanical quantities double subscripts (e.g. d_{ij}) are introduced. The first subscript gives the direction of the excitation, the second describes the direction of the system response.

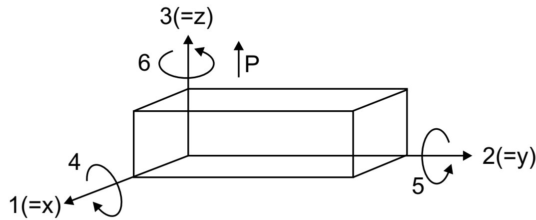

Figure 2.6. Orthogonal system describing the properties of a poled piezoelectric ceramic. Axis 3 is the poling direction

2.3.2 Piezoelectric effect

In order for the piezoelectric effect to occur, the crystal structure has to be non-centrosymmetric as shown in Fig. 2.7.

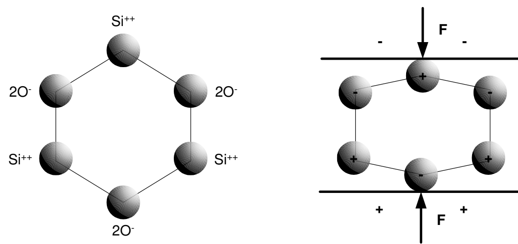

Figure 2.7. Piezoelectric effect

The relationships describing the piezoelectric effect are linear and the coefficients are equal:

$$D_i = d_{ij}T_j \tag{2.6}$$

$$S_j = d_{ij}E_i \tag{2.7}$$

$$i = 1,2,3 \quad j = 1,2,3,4,5,6 \quad ,$$

in which D is the displacement field (or the charge density), T the applied stress, S is the developed strain and E the applied electrical field.

2.3.3 Lead zirconate titanate (PZT)

PZT is the name commonly used for a group of ceramic materials made up of a solid solution of $PbZrO_3$ and $PbTiO_3$. Combining the earlier mentioned piezoelectric equations with the equations describing dielectric relations:

$$D_i = \varepsilon_{ij} E_j \qquad i,j = 1,2,3 \tag{2.8}$$

and elastic relations:

$$S_i = s_{ij} T_j \qquad i,j = 1,2,3,4,5,6 \tag{2.9}$$

results in a matrix describing the complete electro-mechanical behavior of a material. For PZT this matrix becomes:

$$\begin{bmatrix} S_1 \\ S_2 \\ S_3 \\ S_4 \\ S_5 \\ S_6 \\ D_1 \\ D_2 \\ D_3 \end{bmatrix} = \begin{bmatrix} s_{11} & s_{12} & s_{13} & 0 & 0 & 0 & 0 & 0 & d_{31} \\ s_{12} & s_{22} & s_{13} & 0 & 0 & 0 & 0 & 0 & d_{31} \\ s_{13} & s_{32} & s_{33} & 0 & 0 & 0 & 0 & 0 & d_{33} \\ 0 & 0 & 0 & s_{44} & 0 & 0 & 0 & d_{15} & 0 \\ 0 & 0 & 0 & 0 & s_{44} & 0 & d_{15} & 0 & 0 \\ 0 & 0 & 0 & 0 & 0 & 2(s_{11}-s_{12}) & 0 & 0 & 0 \\ 0 & 0 & 0 & 0 & d_{15} & 0 & \varepsilon_{11} & 0 & 0 \\ 0 & 0 & 0 & d_{15} & 0 & 0 & 0 & \varepsilon_{11} & 0 \\ d_{31} & d_{31} & d_{33} & S_{44} & 0 & 0 & 0 & 0 & \varepsilon_{11} \end{bmatrix} \cdot \begin{bmatrix} T_1 \\ T_2 \\ T_3 \\ T_4 \\ T_5 \\ T_6 \\ E_1 \\ E_2 \\ E_3 \end{bmatrix} \tag{2.10}$$

2.3.4 Shear mode displacement

In case of the Xaar actuator, an electric field is applied in direction (2) between the wall electrodes. Using Eq. 2.7 leads to a resulting shear strain S_4 in the stimulated wall. Because of the resulting shear strain, the Xaar actuator function principle is also referred to as the *shear-mode-principle*.

Under the consideration that no external stress is applied to the PZT ceramic, Eq. 2.10 can be reduced to:

$$\begin{bmatrix} S_1 \\ S_2 \\ S_3 \\ S_4 \\ S_5 \\ S_6 \end{bmatrix} = \begin{bmatrix} 0 & 0 & d_{31} \\ 0 & 0 & d_{31} \\ 0 & 0 & d_{33} \\ 0 & d_{15} & 0 \\ d_{15} & 0 & 0 \\ 0 & 0 & 0 \end{bmatrix} \cdot \begin{bmatrix} 0 \\ E_2 \\ 0 \end{bmatrix} \quad \Rightarrow S_4 = d_{15} \cdot E_2 \tag{2.11}$$

S_4 indicates a shear strain around the (1) axis caused by an applied electric field in direction (2). As the actuator walls are clamped at both sides (see Fig. 1.8), the shear strain leads to a chevron shaped deflection.

Chapter 3

Characterization techniques

For the characterization of the piezoelectric actuators different techniques were used. Commercial instruments such as *Fluke* PM6304 RCL-meter and *Hewlett Packard* 4194A Impedance Analyzer are used to measure dielectric permittivity and dielectric losses as functions of frequency and temperature. Tracing of ferroelectric hysteresis P-E loops with a modified Sawyer-Tower circuit was performed to deduce remnant polarizations and coercive fields of the ceramics. To characterize acoustic resonance frequencies and electromechanical coupling factors in each of the channel walls, a novel pulsed technique was employed. Stroboscopic tests were performed to quantify the ultimate inkjet performance: ink-drop velocity, volume, and their angle deviation.

To investigate temperature dependencies, the specimen was placed into a thermostat comprising an oven (a cylindrical metal chamber with heating coils on its outer surface) and a temperature controller, which regulates the temperature inside the oven. The actual sample temperature was measured with a *Keithley* 8 1/2-digit DMM2002 multimeter with built-in linearization for a K-type thermocouple.

To automate the measurements multimeter, temperature controller and measurement instrument were connected to a PC via GPIB bus and RS-232 interface. A *LabVIEW* based routine controls the measurements and saved acquired data into files.

3.1 Dielectric spectroscopy

A *Fluke* PM6304 programmable automatic RCL-meter was used to measure frequency and temperature dependencies of dielectric permittivity *varepsilon* and dielectric loss factor $tan\delta$. The technique is based on simultaneous measurement of the magnitudes of current I, voltage V across the capacitor under test, and the relative phase shift θ between current and voltage. In each measurement cycle the following components are determined:

V_p = Voltage at 0° I_p = Current at 0°
V_q = Voltage at 90° I_q = Current at 90°

From these parameters the following electrical characteristics are calculated:

Impedance:

$$Z = R + iX = |Z|e^{i\phi} \tag{3.1}$$

Resistance:

$$R = \frac{V_p I_p + V_q I_q}{I_p^2 + I_q^2} \tag{3.2}$$

Reactance:

$$X = \frac{V_q I_p - V_p I_q}{I_p^2 + I_q^2} \tag{3.3}$$

Quality factor:

$$Q = \frac{|X|}{R} = \tan\phi \tag{3.4}$$

Dielectric loss factor:

$$\tan\delta = \frac{1}{Q} = \frac{R}{|X|} \tag{3.5}$$

Capacitance:

$$C_p = \frac{1}{\omega(1 + 1/Q^2) \cdot |X|} \quad \text{if} \quad X < 0 \tag{3.6}$$

Phase relations between voltage and current are given in Fig. 3.1a, and between complex impedance, resistance, and reactance in Fig. 3.1b.

The test frequency can be swept from 50 Hz to 100 kHz, where the applied AC-signal is 2.8 V peak-to-peak. A four-terminal (Kelvin) connection is used to minimize insertion losses and to reduce measurement errors. Extended frequency

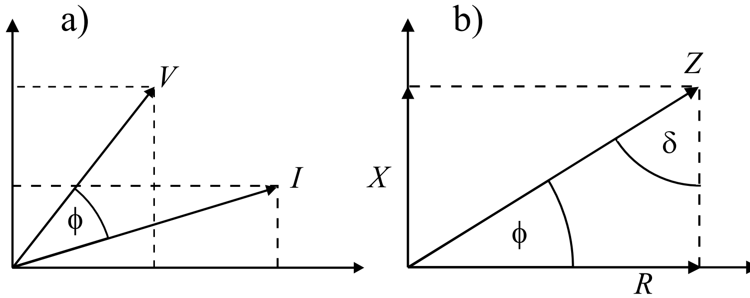

Figure 3.1. Phase relations: a) between the current I and voltage V; b) between the complex impedance Z, resistance R, and reactance X determined with the PM6304 RCL-meter.

spectra (up to 40 MHz) of the channel walls were measured with a PC/GPIB connected HP4194A Impedance Analyzer (Fig. 3.2).

3.2 Manual resonance test

The resonance test is an automated process step after the actuators are produced, whereby only the piezoelectric behavior is regarded. Its aim is to identify and to reject actuators which probably will not have the required printing performance, before they are assembled in the printheads. For experimental purposes it is also possible to carry out a similar test with uncovered actuators on wafer scale in a manual implementation using an HP4194A Impedance Analyzer.

3.2.1 Description

In manual resonance test each case one active PZT channel wall is regarded as an individual actuator. The electrodes on both sides of the wall are connected to the HP4194A (see Figs. 3.2 and 3.3). An AC voltage of 1V is applied within a high frequency band, which lies around the mechanical resonance frequency of a wall. The current and it's phase (with respect to the voltage) are measured within the frequency band. The complex admittance Y, the complex impedance Z and other measures, and their dependency on frequency, can be calculated from the measured data.

$$|Y| = \frac{1}{|Z|} = \frac{I}{V} \tag{3.7}$$

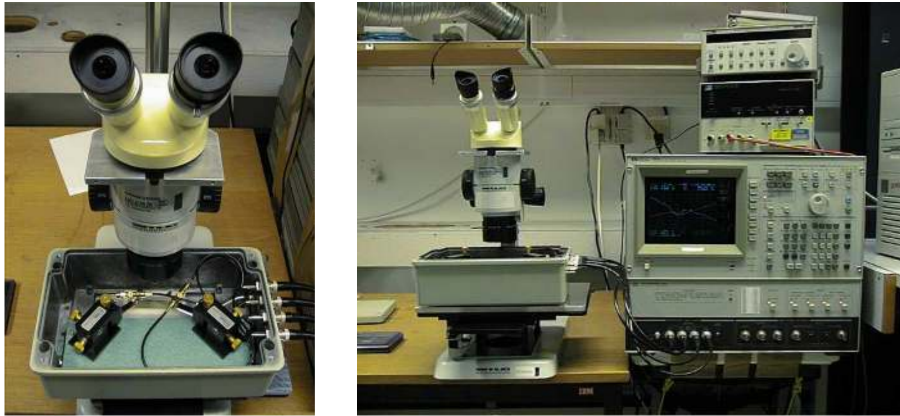

Figure 3.2. Shielded probe station for dielectric characterization of the actuator using *Quater Research* manipulators (left image) connected to an *HP*4194A Impedance Analyser.

3.2.2 Behavior of PZT near mechanical resonance

If a PZT component is driven via the inverse piezoelectric effect and the frequency of the applied electrical field is far from the mechanical resonance frequency, the component will mechanically move according to Eq. 2.11 and force of inertia is negligible. Near to and at the resonance point the amplitude of movement becomes much higher which creates charges due to the normal piezoelectric effect and influences the primary applied field (feedback). Thus the electromechanical performance of a piezoelectric actuator can be measured through simple electrical measurements. An equivalent circuit (Fig. 3.4), which shows the same correlation between admittance and frequency as the actuator, can describe the electromechanical behavior of the PZT walls.

C represents the capacitance between the two electrodes on both sides of the channel in the static case. R_1, L and C_1 correspond to the mechanical properties

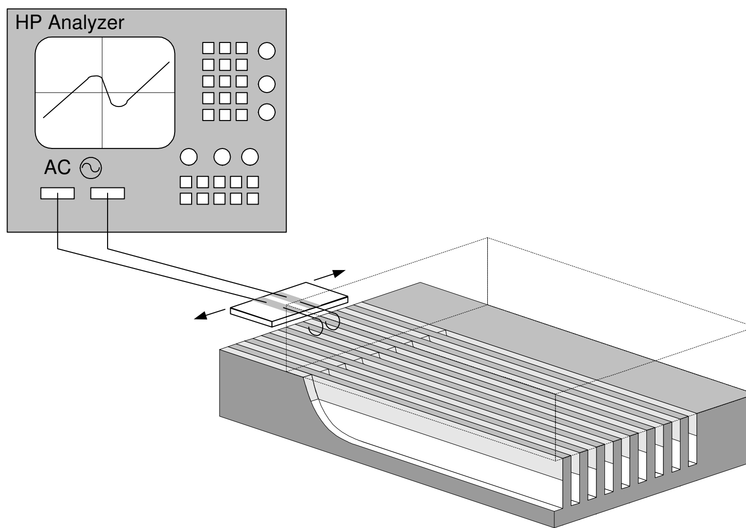

Figure 3.3. Schematic drawing of test rig for manual resonance test

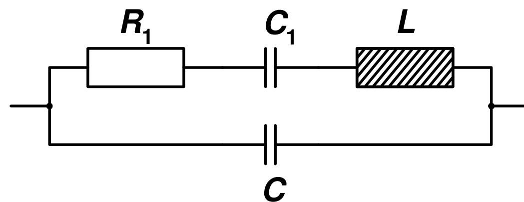

Figure 3.4. Equivalent circuit of the PZT wall

of the piezoelectric oscillator: R_1 represents the mechanical loss, L the mass and C_1 the compliance. The piezoelectric constant and the elastic coefficient of the drive mode (shear mode in this case) as well as geometry can be seen as a transformer between real mechanical measurements and the electrical measurements of the equivalent circuit. The force corresponds to the voltage and the velocity to the current.

A characteristic curve appears (see Fig. 3.5) when the admittance is plotted versus the frequency.

f_s : serial resonance frequency of equivalent circuit (see Fig. 3.4)
f_p : parallel resonance frequency of equivalent circuit
dY : difference of admittance between f_s and f_p

The coupling coefficient k_{15} describes the ability of a piezoelectric ceramic to transform electrical into mechanical energy or vice-versa (the index 15 refers to the shear mode; Fig. 2.6) [30]:

$$k_{15} = \frac{\pi}{2}\frac{f_s}{f}\tan\left(\frac{\pi}{2}\frac{f_p - f_s}{f_p}\right) \tag{3.8}$$

The measured dY and the coupling coefficient k_{15} can be used to estimate the electro-mechanical performance of an actuator. The higher the value of k_{15} and especially of dY, the better is the performance of the actuator. In the normal manufacturing process a robot, which measures 64 channel walls at the same time, does this kind of test and an actuator is rejected if dY falls below a certain minimum value.

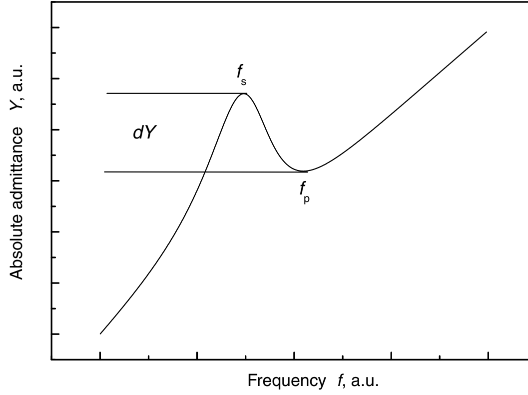

Figure 3.5. Admittance behavior of a piezoelectric actuator near its mechanical resonance.

3.3 Pulsed spectroscopy technique

A new pulsed technique was employed to characterize the piezoelectric effect and the spectrum of resonant acoustic modes in the channel wall (see Paper 1 and Paper 2). The method is based on recording the transient current in the time domain in response to a short voltage pulse applied to the channel wall. Since the investigated PZT ceramics have a high coupling coefficient k_{15}, an electric field applied perpendicular to the polarization will cause a shear displacement shear!displacement of the channel wall. If a voltage pulse with fast rise time is high enough in amplitude to actuate the channel wall, the channel wall will act like a tuning fork and oscillate at resonant frequencies. Because of the piezoelectric effect the mechanical oscillations of the actuating element can be seen as oscillations of the transient current. [31]

The pulsed technique set-up consists of a *GaGe* waveform generator PC-card (2 V meander pulse with 1 µs pulse width generated) and a 54845A *Infinium* Oscilloscope with 1.5 GHz bandwidth and a sample rate of up to 8 GSa/s. Both devices are connected to the channel wall as shown schematically in Fig. 3.6. The whole set-up is designed to have as little parasitic capacitance, inductance and inserted resistance from cables and connections as possible.

Some of the properties derived with the pulsed technique (e.g. the absolute value of the amplitude of the transient current oscillations) require a constant input energy. Therefore, the input voltage V_A was varied with the temperature to keep constant electrostatic energy $\mathtt{E}$:

$$\mathtt{E} = \frac{1}{2}C(T)\ V_A(T) = 1.6 \times 10^{-9}\mathrm{J} \tag{3.9}$$

where C is the channel wall capacitance.

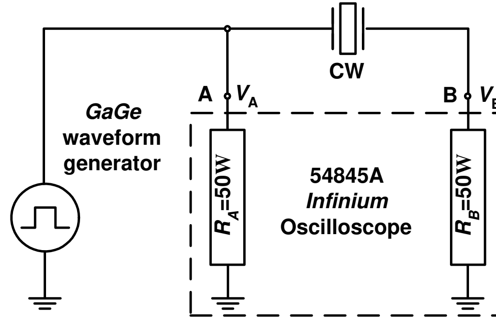

Figure 3.6. Schematic of the pulsed technique set-up to characterize the transient current (recorded in channel B) as a response of the ferroelectric channel wall on a short voltage pulse (traced in channel A).

Fig. 3.7 shows typical data obtained from the transient current. In the plot two important events at different time scales are shown. On the left-hand side of the

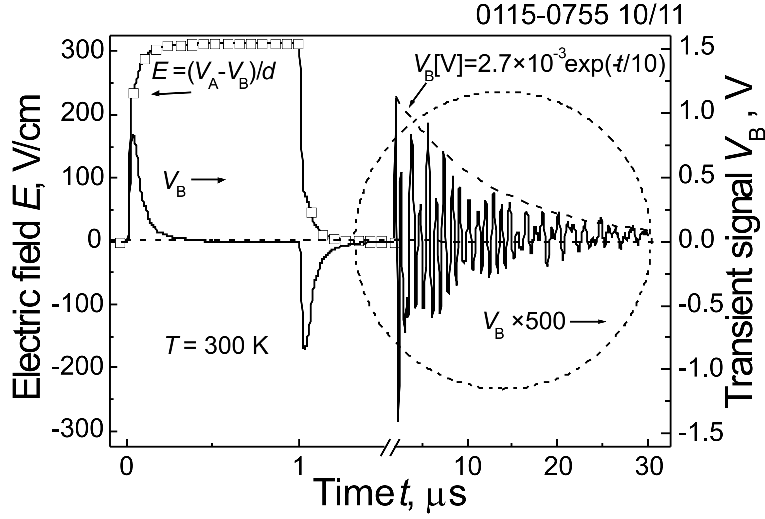

Figure 3.7. Transient response of a channel wall on a short DC voltage pulse. Acoustic oscillations of the transient current signal are seen in ×500 magnification.

axis break ($t = 0$ to 1.5 µs) the processes of electrical charging and discharging of the channel wall can be seen. Here V_A - V_B represents the charging potential, while $V_B/50\Omega$ is the charging/discharging current through the channel wall capacitor (Fig. 3.6). The dielectric permittivity ε' of a channel wall can be expressed through the instantaneous values of V_A and V_B

$$\varepsilon' = \frac{dC}{\varepsilon_0 S} = \frac{d\int_0^t V_B(t')dt'}{\varepsilon_0 S(50\Omega)(V_A - V_B)} \tag{3.10}$$

where V_B is the potential measured at point B in Fig. 3.6, d is the thickness of the wall, $S = 1.59$ mm^2 is the electrode area, and V_A is the input voltage from the GaGe waveform generator card (point A in Fig. 3.6).

On the right hand side of the axis break in Fig. 3.7 (t = 2 µs to 30 µs) the magnified (×500) transient signal V_B is shown. It consists of a combination of several frequencies that are interfering with each other. The amplitude of these oscillations is a figure of merit, which relates the amount of electrical energy fed into the system to the mechanical response. The higher the amplitude, the greater the fraction of the electrical energy converted into mechanical motion. An exponential decay of the transient signal with time is clearly visible as dashed line in Fig. 3.7

Fast Fourier Transform (FFT) of the transient signal in the magnification of Fig. 3.7 gives us the 'main tone' (fundamental resonance frequency) and several overtones as displayed in the spectrum in Fig. 3.8. The plot is normalized to the height of the main resonance.

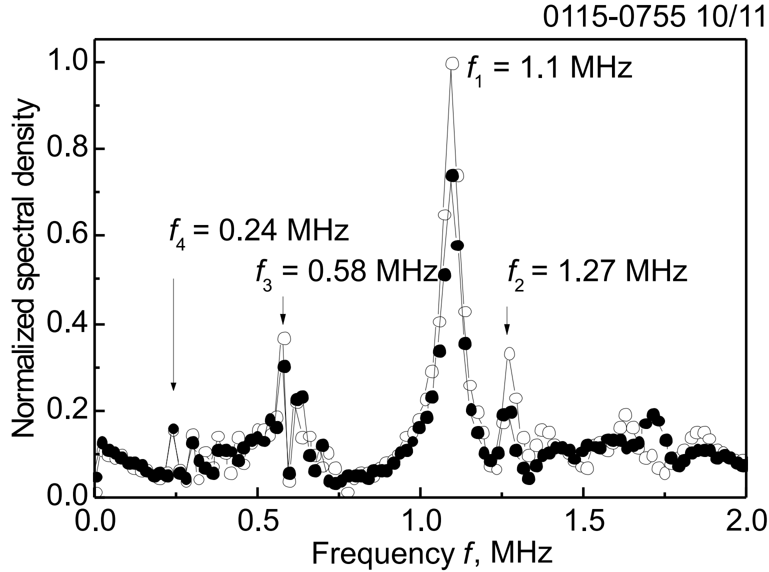

Figure 3.8. Fast Fourier Transform (FFT) of the acoustic oscillations of the transient current signal obtained with the pulsed spectroscopic technique. Only the magnified part in Fig. 3.7 is analyzed.

3.4 Ferroelectric hysteresis *P-E* loop

To record ferroelectric hysteresis *P-E* loops, a triangular signal generated by a function generator was applied to the channel wall. A variable AC-voltage (up to 1 kV) superimposed on a DC-signal supplied by a bipolar operational power amplifier was used to enable saturation of the ferroelectric channel wall as well as to trace minor *P-E* loops. A 'virtual ground mode' modified Sawyer-Tower circuit [32] measures the charge stored in the ferroelectric capacitor by integrating the current required to maintain one terminal of the channel wall at zero volts (see Fig. 3.9). The precision capacitor C_{ref}, used as feedback element in the current integrator, is a key element in obtaining high accuracy with this technique. Our electrometer has 1 pC resolution and was initially calibrated with a *Radiant Technology* RT66A pulsed tester.

An image showing the setup used for *P-E* loop tracing is given in Fig. 3.10.

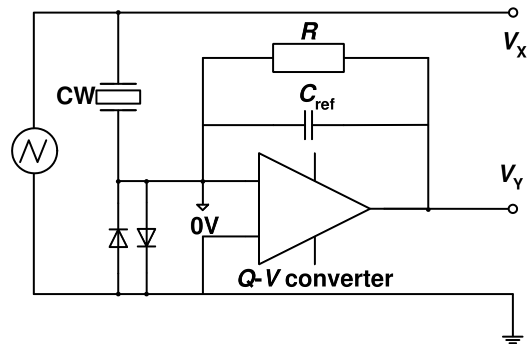

Figure 3.9. Schematic of a 'virtual ground mode' based Sawyer-Tower circuit used for ferroelectric hysteresis loop tracing.

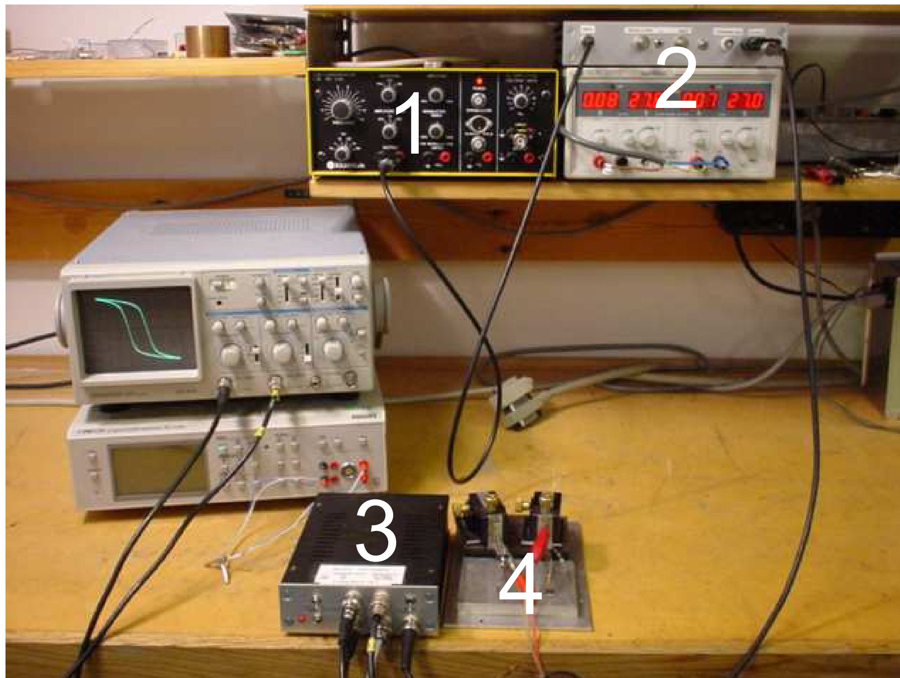

Figure 3.10. Setup for measuring ferroelectric hysteresis comprising a frequency generator (1), an amplifier (2), an electrometer (3), and a probe station (4).

3.5 Stroboscope technique

To investigate how the performance of the piezoelectric ceramic actuator influences on the drop volume and velocity, *stroboscopy* is used. The stroboscope set-up consists of a high-resolution CCD camera, a fixture on which the printhead is mounted, a stroboscope, and a PC with control unit and monitor (Fig. 3.11).

Figure 3.11. The stroboscope setup showing the CCD camera (1) and a mounted printhead (2).

The control unit controls the printhead and the stroboscope, e.g. at a defined instant after the printhead has shot, the stroboscope gives a short light flash and thus an image is produced in which the drop seems to stay fixed in the air. The delay time can be varied with the control unit, which allows the observation of the ink-drop from the very moment of ejection onward. Other parameters such as firing frequency, temperature, and the driving voltage that is applied to the printhead can be adjusted separately. The ejected ink consists of the *lead drop* and, usually, a varying amount of small *satellite droplets* as displayed in Fig. 3.12. The satellites form when the jet becomes that long and thin so the surface tension increases due to the increasing surface-to-volume ratio. The images are recorded with a CCD camera with a magnification of $\times 200$. Horizontal lines at specified distances are drawn on the monitor as measuring marks.

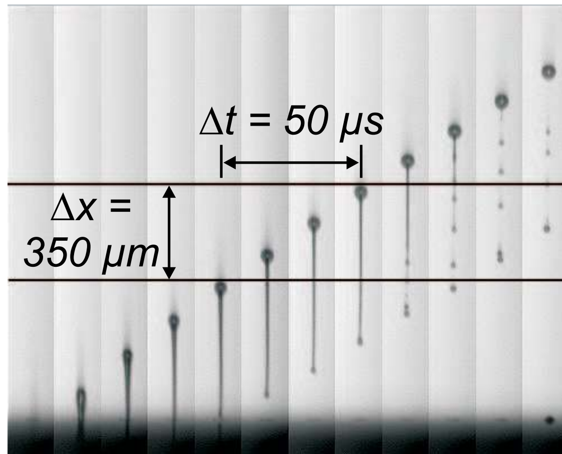

Figure 3.12. Sequence of snapshots at different instants after ink-drop ejection obtained using a stroboscope. One complete firing period is displayed. Generation of satellite droplets after jet break off is very clearly visible. The black bar at the bottom of the image shows the nozzle plate of the printhead.

3.5.1 Drop velocity measurement

When measuring drop velocity, the drop under investigation is moved by adjusting the delay time, so that it coincides with one of the lines drawn on the monitor. The delay time is then increased until the drop reaches the next line. From this delay time increase Δt and the known distance between the two lines Δx, the drop velocity can be calculated by $v = \Delta x/\Delta t$ (Fig. 3.12).

3.5.2 Drop volume measurement

The lead drop volume is measured by focusing the drop at a magnification of about $\times 1700$. Its diameter is measured manually with a caliper and from the known relation between the measured and the real diameter the volume is calculated. To perform the measurement of the total ink jet volume the stroboscope set-up described previously can be used with some modifications. The control unit can be programmed in a way that the printhead prints a specified number of cycles. This and other information, e.g. the number of shooting channels, are given to measurement software in the PC that is connected to a balance. A beaker is placed onto the balance to collect the ink drops. Then the measurement is started. First the average of the values that the balance produces before the printhead shoots, is calculated. Then, weight increase is measured during shooting. After taking the average of the balance's value again, the ejected volume can be calculated from the weight difference and the ink density.

Part II

Our research

Chapter 4

Physical properties of *Xaar* inkjet actuators

During this analysis, the actuators were treated in different ways, such as elevated temperature and high voltage cycling. From this we obtained information on material properties, e.g. the dielectric permittivity and the Curie Temperature. Furthermore, the influence of changes in the actuator geometry on the resonance behavior was investigated.

Details and experimental results are given in Paper 1, Paper 2, Paper 4, and Paper 5.

4.1 Temperature dependence of the dielectric properties

The temperature dependence of the channel wall capacitance (dielectric permittivity) and dielectric loss factor ($\tan\delta$) was measured using the experimental setups for dielectric spectroscopy described in Chapter 3.1 and for pulsed spectroscopy described in Chapter 3.3. For the heat treatment the actuator was placed in an oven as described in the introduction of Chapter 3. Because of the sensitivity of the PZT material to any heat treatment, both measurements were performed simultaneously within the same temperature cycle. The data from the *Fluke* 6304 was recorded continuously over the whole temperature range, while the pulsed technique was measured in 10 °C steps. Fig. 4.1 shows typical temperature dependence of dielectric permittivity and loss $\tan\delta$ for a channel wall.

To deduce the temperature dependence, measurements were made on virgin channel walls and for the same channel walls after the treatment. Applying the Curie-Weiss law (Eq. 2.5) to the reciprocal of the measured capacitance data gave

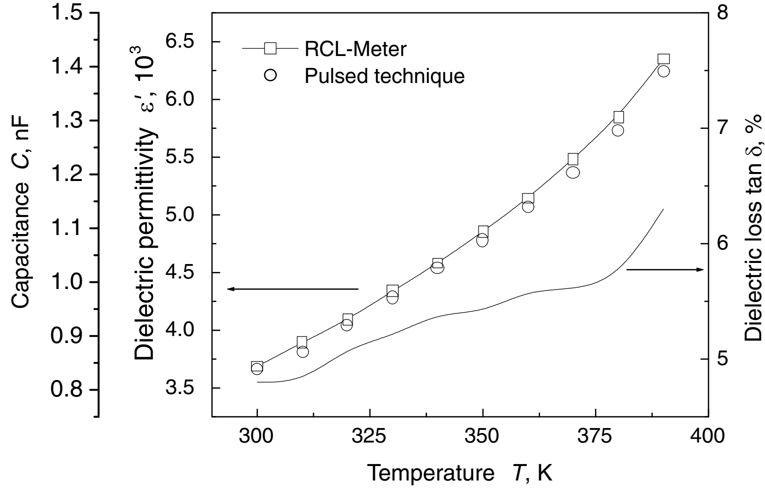

Figure 4.1. Dielectric permittivity and loss factor as functions of temperature measured with RCL-Meter and using pulsed technique.

the Curie temperature of the PZT material. The obtained number of $T_C = 508$ K was comparable with the value given by the manufacturer of 498 K (see Appendix A).

Details on the temperature dependence of the PZT channel walls are given in Paper 1, Paper 2 and Paper 5.

4.2 Frequency dispersion

To measure frequency dispersion of dielectric permittivity and losses the dielectric spectroscopy setup, described in Chapter 3.1, and the pulsed spectroscopy setup, described in Chapter 3.3, were used. The *Fluke* 6304 RCL meter measures in a frequency range from 100 Hz to 100 kHz. Fig. 4.2 displays the dispersion of dielectric permittivity and loss $\tan\delta$ for a channel wall at 300 K and 380 K. To investigate at higher frequency ranges, from 1 kHz to 15 MHz, an HP4194A Impedance Analyzer was used (Fig. 3.2). The most interesting frequency range is around 1 MHz, since within this range the main resonance frequency of the channel walls can be found. In Fig. 4.3, the dielectric permittivity of a virgin and a heat treated channel wall is plotted. Besides the main resonance, several subharmonics are clearly visible.

Detailed discussions on the obtained results are given in Paper 1, Paper 2 and Paper 5.

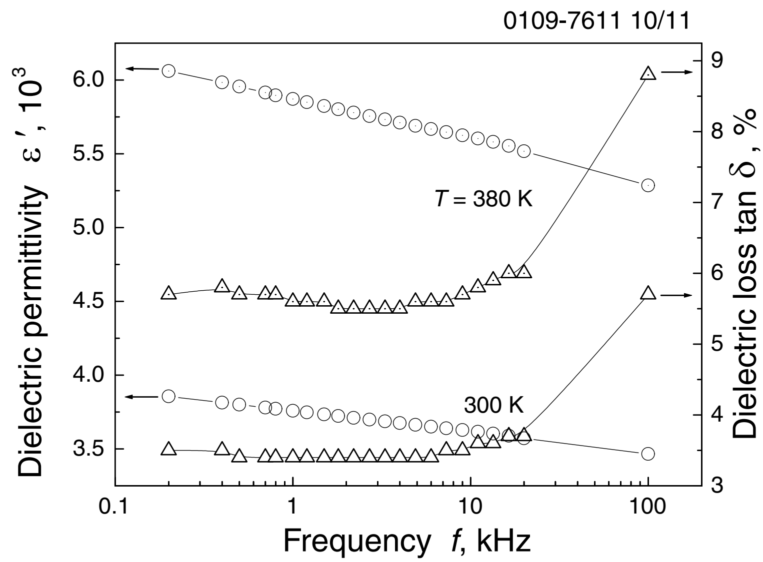

Figure 4.2. Frequency dispersion of the dielectric permittivity and dielectric loss at 300 K and 380 K measured with *Fluke* 6304.

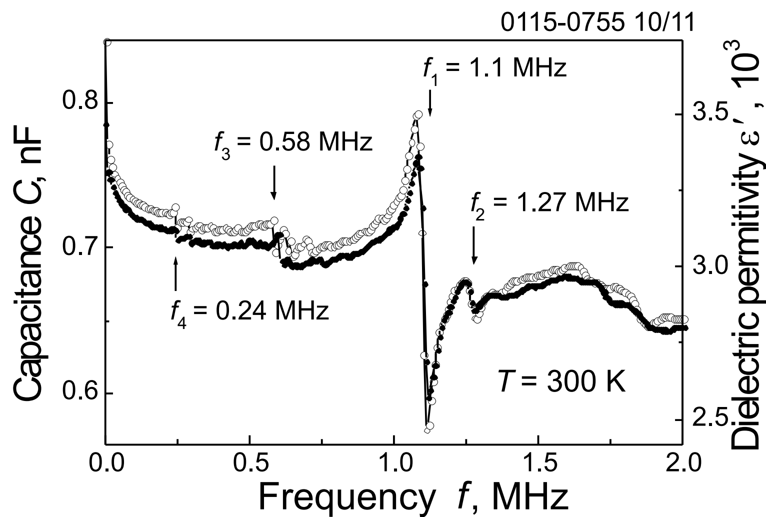

Figure 4.3. Dispersion of dielectric permittivity measured with a HP4194A in the frequency range from 1 kHz to 2 MHz. The resonance frequency and several subharmonics are clearly visible.

4.3 Ferroelectric fatigue

Ferroelectric hysteresis loop tracing, as described in Chapter 3.4, gives information on the polarization of the PZT material. High electric fields are needed to induce saturation polarization of the channel walls. Cycling the electric field (triangular signal of 88.5 kV/cm, 50 Hz) leads to a decrease in polarization. The decrease of the remnant polarization as function of the number of cycles is displayed in Fig. 4.4a.

Reason for this is the electrode arrangement in the actuator. In the *Xaar* actuator case the electric field is applied perpendicular to the polarization direction. Thus, during cycling the electric field, 'weak' dipols will rotate to be aligned in field direction.

Investigation of a virgin channel wall with a polarization microscope showed a homogeneous polarization over the whole top surface ('1' in the right panel of Fig. 4.5). Channel wall '2' is a neighbouring wall experienced the high electric field. After the treatment the polarization pattern of the element has changed. In polarised light clusters of grains along the PZT - Al interface appear brighter than grains in the middle of the top surface. After grinding the top of the element by approximately 20 µm the clusters disappeared and the top surface becomes homogeneous like the virgin element. The electric field applied during the treatment was 88.5 kV/cm, so, high enough to polarize the element. Since the virgin element was already polarized in perpendicular field direction the high voltage treatment initialised a reorientation of the ferroelectric dipoles towards the direction of the field. This is visible in polarised light as clusters. The investigated clusters appeared very bright; therefore 90° rotation of the light is assumed which coincides with a dipole reorientation of 90°. The reorientation starts at the PZT-Al interface at the top surface of the element. At that position the grains were not clamped as much as in the middle of the ceramic. Evidence for this is the non-changed area in the middle of the top surface and that the grinded surface did not show any reoriented grains at all.

Another observation was, that applying Eq. 4.1 to the array of $P - E$ loops we succeeded to envelop all loops into one major loop (the initial loop) as shown in Fig. 4.4b.

$$E_{\text{eff}} = (E - 4\pi P \times \alpha) \times \beta \qquad (4.1)$$

α, β and P_r as functions of the number of cycles are displayed in the insert to Fig. 4b. The exact role of the coefficients α and β is still not clear to use and will be further investigated.

More details on ferroelectric fatigue are given in Paper 2 and Paper 5.

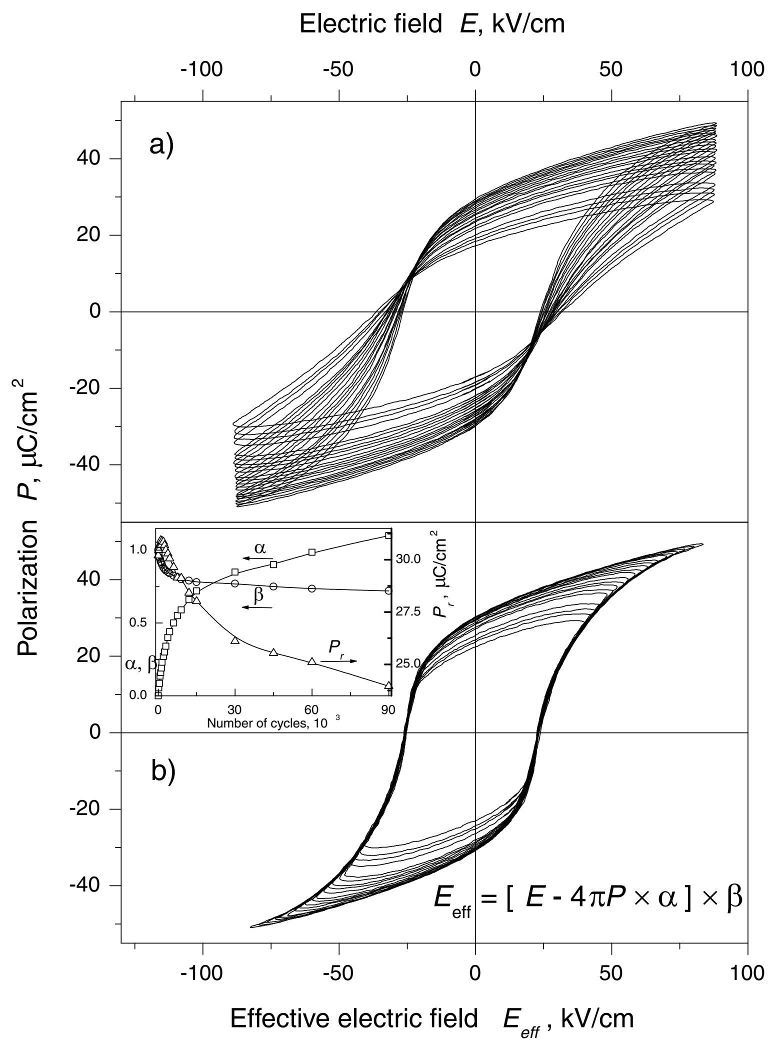

Figure 4.4. a) A series of ferroelectric hysteresis loops obtained with a modified Sawyer-Tower circuit. With increasing number of cycles (1 to 90,000) the remnant polarization decreases and the coercive field increases. b) Applying Eq. 4.1, all loops envelop into one major loop. Insert: α, β and P_r as functions of the number of cycles

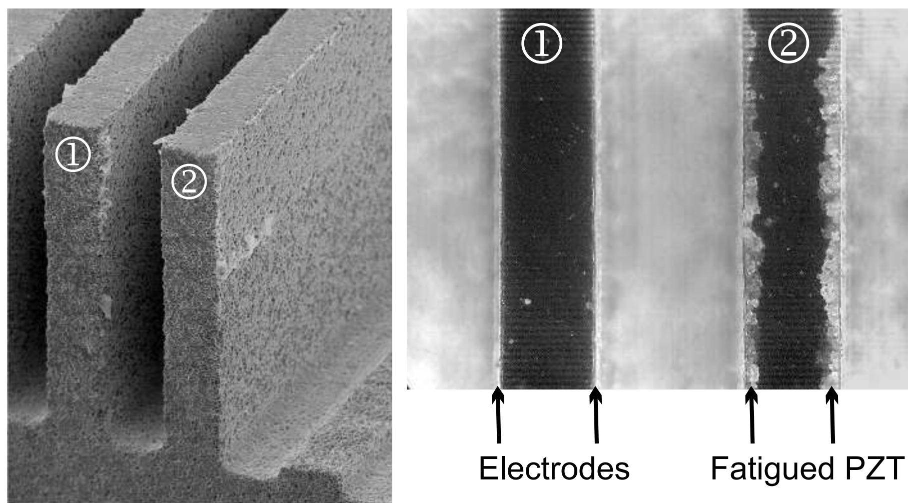

Figure 4.5. Left panel: SEM micrograph (×300) of an array of micromachined channel walls. Right panel: Optical microscope image taken in polarized light showing a virgin element '1' and an element '2' treated by a triangular signal of $E =$ 88.5 kV/cm at 50 Hz. The treated wall shows clearly a fatigued area close to the electrodes on both sides.

4.4 Acoustic resonance modes

Two different approaches were made to investigate resonance modes of the actuator. The first one, the manual resonance test, uses an HP4194A Impedance Analyzer shown in the dielectric spectroscopy set-up (Chapter 3.1) and is explained in detail in Chapter 3.2. The other method is based on the pulsed spectroscopy which is described in Chapter 3.3.

As shown in Fig. 4.3, there are several additional subharmonics beside the main resonance at 1.1 MHz. To clarify the nature of these resonance modes, a spectroscopic study on a specially made actuator was made. The actuator was diagonally cut to get an array of 128 channel walls of different lengths: from 4.3 to 10 mm (Fig. 4.6. The 'short' channels walls have a variable height and a non-clamped top. The 'long' channels have 360 µm high channels walls clamped on bottom and top. The resonance characteristics of the 128 channels is given in Fig. 4.7.

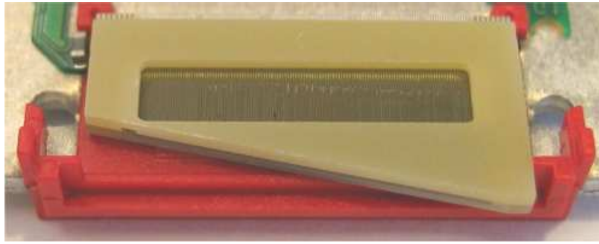

Figure 4.6. Specially made actuator with 'short' (4.3 mm) and 'long' (10 mm) channels.

As clearly seen, there are eight weak low-frequency resonance peaks whose positions do not depend on the channel wall length, whereas there are two resonances at frequencies between 1.0 and 1.2 MHz which change their amplitude and position at different channel lengths. With channel elongation these two resonances come closer, merge together and form a single strong resonance peak at 1.1 MHz.

To get an idea on the parameters which control the acoustic spectra and on a frequency scale, one can consider the vibrations of the walls as oscillations of a slender beam with different boundary conditions at the edges. Resonance frequency of different modes $\eta_{i,n}$ can be found in [31]:

$$f_{i,n} = \frac{1}{2\pi}\frac{d}{h^2}\sqrt{\frac{E}{12(1-\nu^2)\rho}\eta_{i,n}^2} \quad , \tag{4.2}$$

where index i stands for the acoustic mode type, while n is the mode number, d is the thickness and h is the height of the channel wall, E is the elastic modulus, ν is the Poisson ratio and ρ is the mass density. Bottom clamped channel walls oscillate as cantilevers and the first two modes are:

$$\eta_{I,1} = 1.875, \quad \eta_{I,2} = 4.694.$$

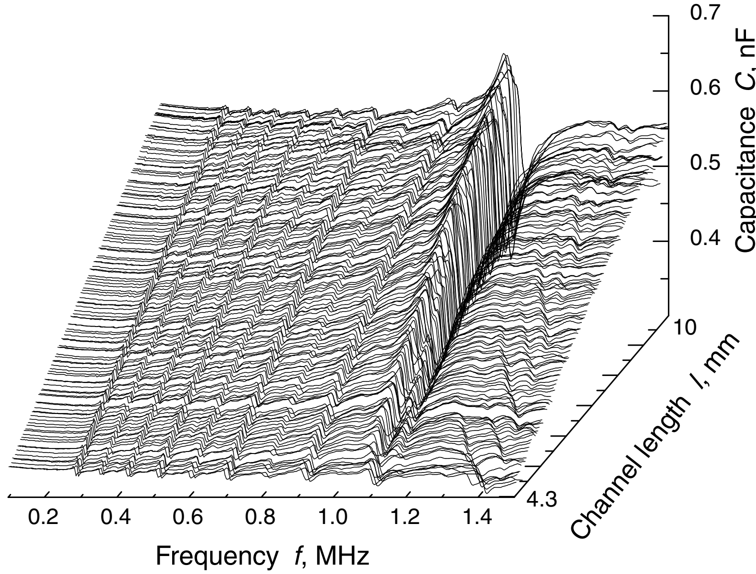

Figure 4.7. Capacitance-frequency ($C-f$) characteristics of an array of 128 channel walls of different length (4.3 to 10 mm).

The fundamental mode of both, bottom- and top-clamped walls is:

$$\eta_{II,1} = 4.730.$$

Although the Eq. 4.2 gives a very crude approximation to the real channel wall spectra, they describe the main observations in Fig. 4.7. We believe that the first eight features are the cantilever-type. They come from the shallow part of channels with non-clamped tops. This part of the channel walls is similar in both, 'short' and 'long' channels thus the resonance frequencies are the same for the whole array. Eq. 4.2 does not give all the resonance modes since the channel walls have variable height, however it shows the correct order of the resonance frequencies as well as dependence on the thickness d and thickness-to-height d/h aspect ratio. The next two resonance features between 1 and 1.2 MHz in the 'short' channels we identify as $f_{I,2}$ and $f_{II,1}$ resonance modes. They are very close since $f_{II,1}/f_{I,2} = 1.015$, and with channels elongation/deepening the frequency $f_{II,1} \propto 1/h^2$ decreases and merges to $f_{I,2}$.

The resonance spectra are complicated due to spurious oscillations and, as fingerprints, vary between actuators. Many issues should be accounted to make quantitative spectra analyses: variable channel depth, different compliance of the supports at the built-in and top-glued ends of the channel walls, the effects of sawing damage, effects of electrical polarization, etc.

Observations made with the pulsed spectroscopic technique are given and discussed in Chapter 3.3 and in Paper 1, Paper 2, Paper 4, and Paper 5.

4.5 Correlation with inkjet performance

The setup given in Chapter 3.5 is used to correlate properties of the channel walls to the performance of the printhead. The influence of high voltage and temperature treatments could be revealed in this way as shown in Fig. 4.8. If possible, only part of the whole channel wall array was treated to keep the non-treated part as reference.

Experimental results are given in Paper 4 and Paper 5.

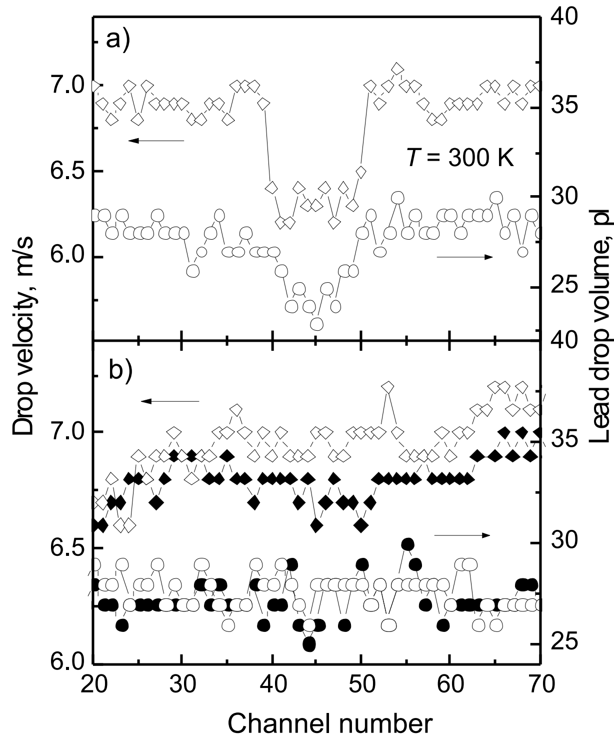

Figure 4.8. Degradation of drop velocity and lead drop volume due to a) high voltage treatment, b) temperature treatment.

Chapter 5

Thermometry inside inkjet actuators

The possibility is investigated to use the capacitance of the channel walls as a temperature sensor. This chapter describes equipment made to measure the capacitance of the channel walls and describes some measurements that were made to check the functionality of the equipment and to investigate the magnitude of temperature changes inside the actuator.

I started the research on this topic already in April 1999 as subject of my Master's Thesis [33]. The research was continued and refined in the beginning of my Ph.D. studies. Onne Wouters from the University of Groningen, The Netherlands and Andreas Jorzick, *XaarJet AB*, joined the research partly in 1999 respectively 2001.

The results are published in Paper 3, in WO Patent no. 02/26500, and [34].

5.1 Introduction

Temperature compensation is necessary to enable a constant drop velocity throughout the whole temperature range of the operating printhead (10 °C - 60 °C). The drop velocity depends on the viscosity of the printed fluid. As the viscosity of the fluid has a temperature dependency, the velocity of the ejected droplets is also temperature dependent. Regulation of the temperature inside the printhead to control the viscosity of the fluid and therefore the drop speed is not possible. But it is possible to control the driver voltage of the printhead. This driver voltage is responsible for the movement of the channel walls.

In the standard XaarJet printhead, a thermistor is used to regulate indextemperature!regulation the driver voltage depending on the temperature close to the actuator. Investigations of the temperature distribution inside the printhead have proved that the temperature measurement with the thermistor is not sufficient for

a fast and precise regulation of the drop velocity [33]. The goal was to improve the temperature compensation by using the walls between the dummy channels as temperature sensitive elements inside the actuator (Fig. 5.2). The linear temperature behavior of the capacitance of the dummy channel walls in the operating temperature range was demonstrated in experiments (Fig. 5.1). With this knowledge, a new temperature compensation circuit based on a voltage divider as a metrology technique was built up. Finally, experiments proved that the temperature compensation circuit works in a proper manner and gives the expected results for linear temperature compensation.

5.2 Theoretical background

5.2.1 Temperature compensation

During printing the temperature inside the printhead changes. The major heat sources are the driver chips, the actuator and the electrical components of the PCB (printed circuit board). To remove most of the heat, the chips and the PCB are glued onto an aluminium base plate. The base plate temperature can be controlled by an external cooling system. The amount of heat produced depends on the firing frequency and the number of firing channels. If the printhead is firing 100%, most heat will be generated. During normal printing the firing frequency and the number of firing channels are changing and therefore the temperature inside the printhead, especially inside the actuator, fluctuates. Temperature fluctuations of the actuator also causes fluctuations of the ink temperature. The ink viscosity shows a temperature dependency, which can be explained by the strength of the atomic bonding between the ink molecules. At higher temperatures the oscillation of the ink molecules is lager and the strength of the atomic bonding is reduced. The viscosity of a typical oil-based ink for example decreases from 11 to 8 mPa·s with temperature increase from 30 to 40 °C. Less of the force, exerted onto the ink due to the deflection of the channel walls is necessary to break the atomic bonding of the ink molecules. Therefore more of the force will be transformed into the velocity of the ink drops. If not compensated the viscosity variations would lead to significant changes in drop velocity and volume, 9% and 13%, respectively, as measured with Xaar-type actuators [20]. A regulation of drop velocity and volume can by performed by matching the driver voltage to the temperature inside the printhead.

5.2.2 Existing temperature compensation

In the standard XaarJet printhead the temperature compensation is achieved by regulating the driving voltage ($V100$) with a thermistor (R_{therm}). This thermistor

is placed close to the actuator (Fig. 5.3). The electrical behavior of R_{therm} as a function of temperature T is given from the manufacturer as:

$$R_{therm} = 10^5 \cdot e^{3700[1/(T+273.15)-1/298.5]} \tag{5.1}$$

R_{therm} is part of the temperature compensation circuit, which is implemented on the PCB together with the driver chip. This circuit generates and regulates the $V100$ signal.

$$V100 = V_{(chip)} \cdot R_7 \cdot (1 + R_{therm}/R_2)/(R_8 + R_7) \quad , \tag{5.2}$$

where R_2, R_7 and R_8 are as well parts of the compensation circuit. $V_{(chip)}$ is adjusted for each printhead to make all printheads have the same average drop velocity.

If the temperature of the actuator increases the temperature of the thermistor also increases and R_{therm} will decrease (Eq. 5.1). $V100$, which is proportional to R_{therm}, will therefore also decrease. A decrease of $V100$ lowers the wall motion and the drop speed is reduced. In this way drop speed as a function of the actuator temperature is kept constant.

The big draw back with this kind of temperature compensation is the high time constant of the sensing element.

5.2.3 Temperature dependence of channel wall capacitance

A channel wall covered with electrodes can be viewed as a common plate capacitor whose capacitance is given by:

$$C = \frac{\varepsilon \cdot A}{d} \tag{5.3}$$

where ε is the dielectric constant of the PZT material, A the electrode surface area and d the thickness of the wall.

Writing $x \cdot y$ for A and differentiating with respect to temperature gives:

$$\frac{\partial C}{\partial T} = \frac{xy}{d}\frac{\partial \varepsilon}{\partial T} + \frac{\varepsilon y}{d}\frac{\partial x}{\partial T} + \frac{\varepsilon x}{d}\frac{\partial y}{\partial T} - \frac{\varepsilon xy}{d^2}\frac{\partial d}{\partial T} \tag{5.4}$$

$$\Rightarrow \frac{1}{C}\frac{\partial C}{\partial T} = \frac{1}{\varepsilon}\frac{\partial \varepsilon}{\partial T} + \frac{1}{x}\frac{\partial x}{\partial T} + \frac{1}{y}\frac{\partial y}{\partial T} - \frac{1}{d}\frac{\partial d}{\partial T} \tag{5.5}$$

Assuming an isotropic linear thermal expansion coefficient α_l this equation reduces to:

$$\frac{1}{C}\frac{\partial C}{\partial T} = \frac{1}{\varepsilon}\frac{\partial \varepsilon}{\partial T} + \alpha_l \tag{5.6}$$

Fig. 5.1 shows the capacitance of channel walls for different temperatures.

The relative capacitance change is about $5 \times 10^{-3}/^{\circ}\mathrm{C}$, which is much higher than the value for the linear thermal expansion coefficient, which is given as $7.7 \times 10^{-6}/^{\circ}\mathrm{C}$. Therefore thermal expansion may be neglected resulting in:

$$\frac{\partial C}{\partial T} \propto \frac{\partial \varepsilon}{\partial T} \tag{5.7}$$

From the Curie-Weiss law (Eq. 2.5) we know that in general there is no linear relationship between dielectric constant and temperature, but the largest non-linearity occurs around the Curie temperature and normal operating temperatures are well below that. Fig. 5.1 shows that assuming a linear relationship between the channel wall capacitance and temperature is justified in the temperature range of normal operating.

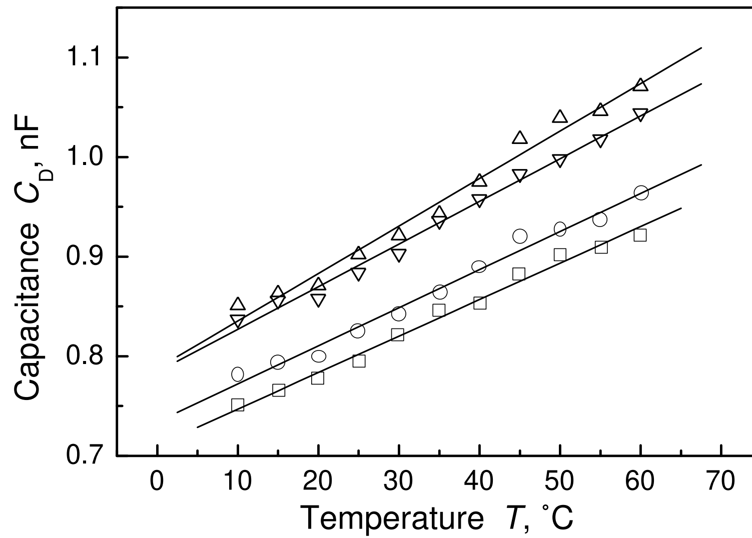

Figure 5.1. Electrical capacitance of individual dummy walls versus temperature.

5.3 Experimental setup

5.3.1 Modification of the printhead

In every actuator four extra channels are sawn, two on each side. These channels are not used for drop generation but are made to give the first real firing channel the same characteristics as the channels in, for instance, the centre of the actuator. These so called 'dummy channels' are used in the temperature measurements (Fig. 5.2).

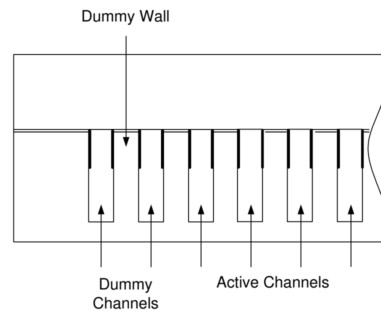

Figure 5.2. Actuator cross section and 'dummy wall'

It is not possible to solder a wire manually onto the bond pad on the back side of the actuator. Instead, two bigger bond pads have to be placed somewhere near the actuator (Fig. 5.3). Using a wire bond these larger pads were connected with the pads on the actuator and larger wires can be soldered to the bigger pads and taken out off the printhead.

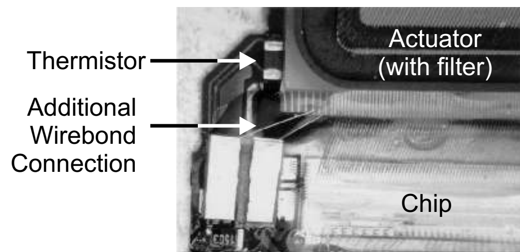

Figure 5.3. Image showing the position of R_{therm} and the additional wirebond connections for electrical connection of the dummy walls

5.3.2 Electronics

A voltage divider circuit, shown in Fig. 5.4, was chosen to monitor the capacitance C_D of a dummy wall. The dummy wall was connected in series with an external,

discrete capacitor C, which was kept at constant temperature. For the input voltage V_{osc} we used a stable AC-signal of 4.0 kHz, with 10 V amplitude. At this frequency minimum noise was found in a previous analysis. We found C = 20 nF to be well matched to dummy wall capacities of typically 1 nF to provide an essentially linear, but sensitive output voltage V_1 in the temperature range of interest, 20 to 60 °C. A high impedance voltage follower was used to decouple the capacitors C_D and C from the rest of the circuit. With a band-pass filter of 4 kHz resonance frequency and 440 Hz bandpass we reduced noise from the neighboring channels during printing. The signal was then converted into a DC-signal. A low-pass filter with a cut-off frequency of 500 Hz reduced residual noise, which passed the band-pass filter. The resulting DC-signal could be recorded to monitor temperature changes of the dummy wall.

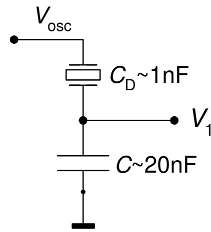

Figure 5.4. The voltage divider circuit

The output signals were connected to an HP34970A Data Acquisition unit. Together with the special software belonging to it, this unit was used to log all the data from the temperature measurements.

5.4 Measurements

5.4.1 Calibration

Calibration of the dummy wall thermometer was carried out in a climate chamber. For the following experiments we used Xaar Jet XJ128 printheads with dummy wall thermometers at both ends of the actuator. We refer to these as 'dummy wall L' at the left-hand side of the actuator, next to active channel 1, and 'dummy channel R' at the right-hand side, respectively. The DC-output voltages for both dummy walls were recorded while the climate chamber temperature was raised in steps of 5 °C. Typical calibration curves for the two dummy walls of a printhead are given in Fig. 5.5, indicating the high sensitivity of these dummy wall thermometers.

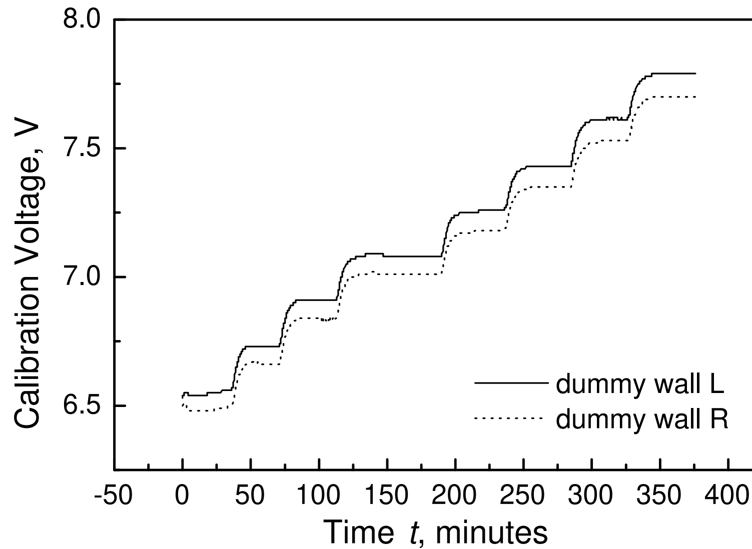

Figure 5.5. Typical calibration curves of dummy wall thermometers.

5.4.2 Temperature differences induced by ink flow

To get a feeling on the actual temperatures inside the actuator, a printhead was fired under different circumstances. A measurement consisted of firing the printhead at 100% (all 128 channels) for 20 minutes and then changing the pattern to firing 'zero signals' on all channels again for 20 minutes. In this mode the chip will be running but not produce droplets. Thereafter, the driving voltage to all channels will be turned off while continuing measuring the temperature.

Fig. 5.6 shows the result for temperatures obtained for left and right dummy channel walls.

When the same experiment was repeated with ink fed into the printhead the temperature development of Fig. 5.7 was obtained. The ink had a twofold effect. On the one hand the saturation temperature with 100% firing was considerably lowered in comparison with 'dry printing' indicating the cooling effect of the ink. On the other hand we observed a temperature difference of some 2 °C between the two ends of the actuator. This was due to the ink inlet being located at one side of the actuator, and the ink being heated up within the ink manifold when flowing to the ink channels at the other side of the actuator.

The results on this measurement are evaluated in Paper 3.

5.4.3 Temperature differences induced by print pattern

A series of measurements was made to see how large the temperature difference can become between parts of the actuator that are firing and parts that are not

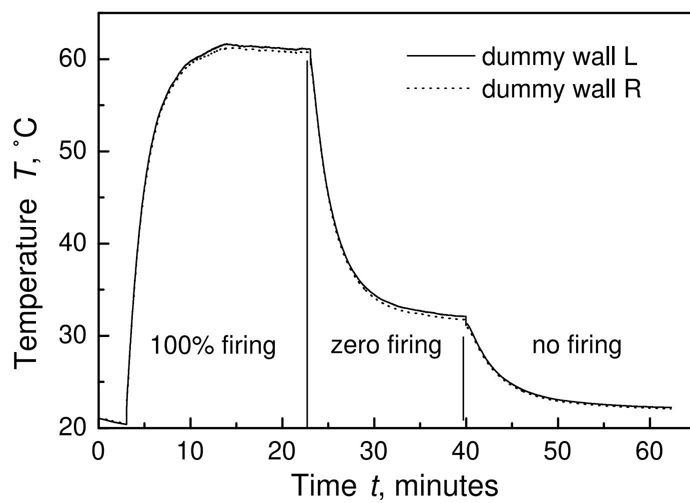

Figure 5.6. Temperatures at both ends of the actuator when printing without ink

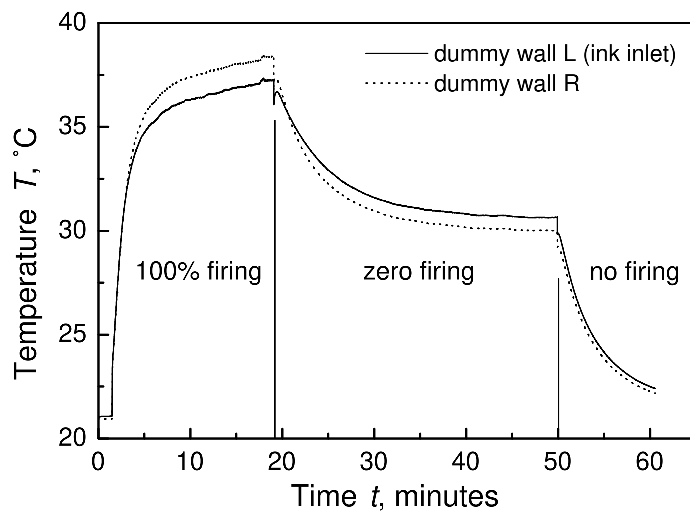

Figure 5.7. Temperatures at both ends of the actuator when printing with ink

firing. These measurements were made not only with the standard printhead (results shown in Fig. 5.9) but also with a printhead, on which the cover material has been changed from PZT to aluminium nitride (AlN) (Fig. 5.10). This material has almost the same mechanical characteristics as PZT but has a much higher thermal conductivity. The AlN-cover could therefore be used to even out temperature differences inside the actuator.

For a measurement the actuator is divided into four parts of 32 channels each. For the first half hour the printhead is firing part 1 (channels 1 to 32) and then the pattern is switched to part 2, ten minutes later to part 3 and again ten minutes later to part 4 (Fig. 5.8).

More detailed results on this measurement can be found in Paper 3.

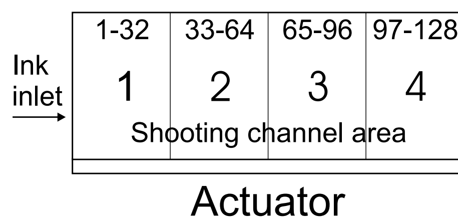

Figure 5.8. Sketch of the actuator showing the four areas of firing channels. The ink inlet is on the left side of the actuator.

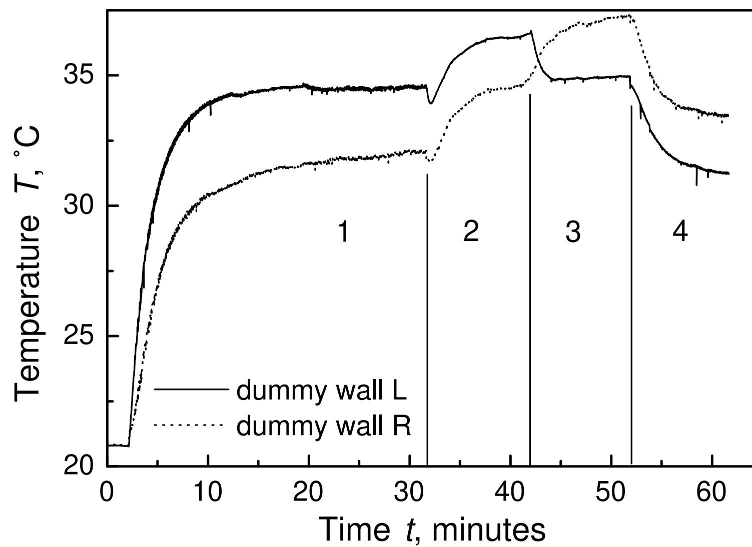

Figure 5.9. Temperatures at the two ends of a standard actuator for different print pattern.

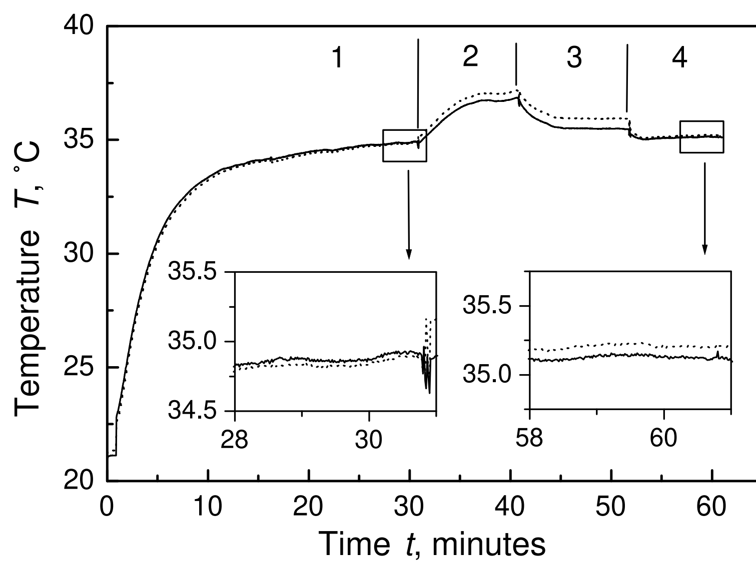

Figure 5.10. Temperature equilibration by usage of high thermally conducting material (AlN) as cover.

5.5 Conclusions

- The results of the calibration again show the linear relation between the capacitance of the channel walls and their temperature. The large differences between calibration results of different printheads, makes it necessary to calibrate every printhead before measurements are made.
- Fig. 5.6 shows that the output voltage follows temperature changes very rapidly and the fact that the calculated temperatures for the two signals in Fig. 5.6 stay exactly the same, indicate that the calibration is very accurately.
- When the printhead is printing ink, the temperature decreases significantly as shown in Fig. 5.7. The cooling effect of the ink flow is large.
- Fig. 5.9 shows that in a normal printhead clear temperature differences can occur if a very asymmetric pattern is fired for a long time. It is strange that the temperature measured on the right side of the printhead is higher when firing pattern 2 than it is firing pattern 1. A measurement of the current going into the printhead shows that the total power consumption of the printhead is lager when patterns 2 and 3 are fired. This can be caused by an larger average capacitance on the centre channels in the actuator.
- These differences almost completely disappear when a cover of aluminum nitride is used (Fig. 5.10). It seems that using this cover is a good way to insure equalization of the temperatures over all the channels.

Chapter 6

Chevron-type inkjet actuator

From the beginning of the Xaar shear mode concept, the idea of making a Chevron type actuator existed. The Chevron actuator would use the whole channel wall as active part instead using just the upper half as the standard actuator. This would make the printhead much more powerful and should lead to less power consumption and therefore less heat dissipation.

Onne Wouters from the University of Groningen, The Netherlands, Thomas Jäger [35] from Albert-Ludwigs-University of Freiburg, Germany and Gerald Richter from Chemnitz Technical University, Germany, joined the research partly in 1999, 2002 and 2003, respectively.

The results were published in Paper 6 and are submitted to the European Meeting on Ferroelectrics EMF 2003, Cambridge, UK.

6.1 Introduction

The standard Xaar actuator consists of a non-polarized cover plate with the ink inlets and a polarized base plate with walls and channels. All the walls of a channel wafer are completely polarized in one direction. To be able to bend the wall properly only a part of the wall should be active. Therefore the upper part of each wall is plated with aluminium electrodes. From calculations and experiments an electrode depth of 43% is found to be the optimum for drop ejection.

To improve Xaar actuators in respect of print performance and power consumption, Chevron design is proposed. Figs. 6.1 show in simplified cross section sketches the main constituents of (a) a standard XJ128 actuator and (b) an actuator of Chevron design. As displayed, the Chevron actuator includes an additional PZT layer with polarization in opposite direction of the base plate polarization. Furthermore, the depth of the aluminium electrodes is increased, thus they cover the channel walls completely from top (where the cover plate is attached) to bottom of the channel.

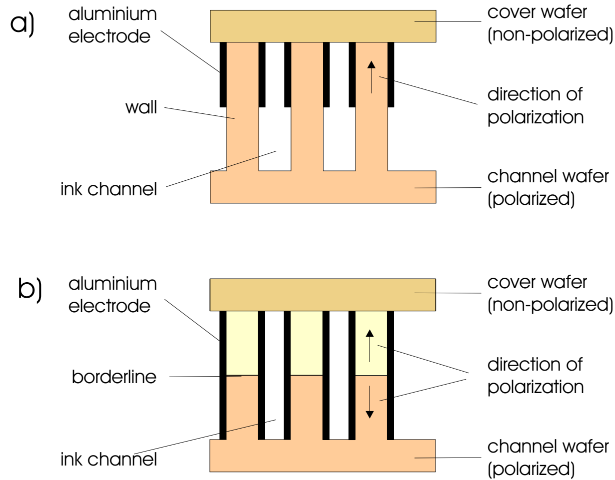

Figure 6.1. a) Standard Xaar design versus b) Chevron design

There are two possibilities to construct Chevron actuators:

1. Producing a Chevron wafer sandwich composed of two single wafers with opposite poling direction joint together by means of a gluing process, followed by sawing of channels into this compound (later called *Laminated Chevron*).

2. In-situ polarization reversal of the lower part of the walls after channel sawing into a monolithic wafer (later called *Monolithic Chevron*).

In the following section both designs will be reviewed and manufacturing possibilities are shown.

6.2 Laminated Chevron design

In the case of laminated Chevron actuators, the channelled component consists of two layers of PZT material having their polarization in opposite directions. Fig. 6.2 depicts this layer structure in an SEM micrograph of a cross section of a Chevron actuator.

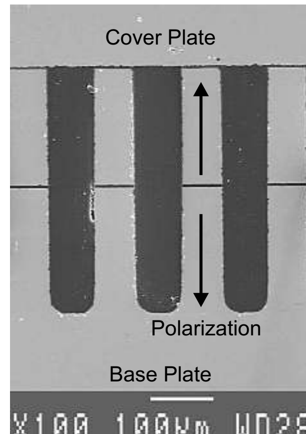

Figure 6.2. SEM micrograph of a laminated type Chevron actuator. The polarization directions in the base plate are indicated by arrows. The glue joint is visible as horizontal lines in the middle of the channel walls.

6.2.1 Manufacturing

The manufacturing of the Chevron wafer sandwiches involves process steps as indicated in Fig. 6.3 and in the process flow beneath.

polishing
⇓
laminating
⇓
bonding
⇓
pre-inspection
⇓
dressing
⇓
inspection

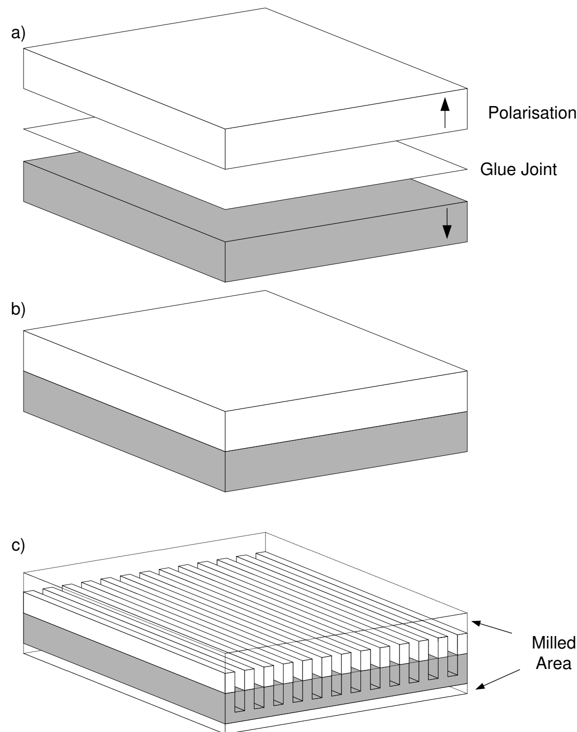

Figure 6.3. Process flow visualizing the manufacturing of a 'laminated Chevron' wafer sandwich.

Polishing Before the PZT wafers are bonded together to build a Chevron sandwich each of them must be polished on the bonding side. Previous tests showed that bonding of non-milled surfaces leads to a decrease in the efficiency of the actuator.

Laminating The lamination process is done in a cleanroom environment to ensure that no particles will be enclosed between the wafers. Embedded particles create high local stress which in the worst scenario destroys the wafer sandwich. For the lamination itself, a thin layer of epoxy-like adhesive is applied to the polished surface of one of the wafer by means of a stamping process. Through the stamping, good control over homogeneity and thickness of the glue joint is given.

Bonding Wafer bonding is carried out directly after the lamination, since the adhesive has a limited dwell time of two hours. After lamination the polished surfaces of the wafers are brought together by hand and slightly pressed together. To get a good bond, i.e. high bond strength, the sandwich is placed in a temperature

controlled pneumatic press. There, a constant temperature of 100 °C and a pressure of 2 bar is applied for 15 minutes to the wafers.

Pre-inspection After bonding, the wafer sandwiches are inspected for damages, i.e. cracks or broken edges. Also sandwiches with a wafer-to-wafer misalignment are rejected.

Dressing Since the as-bonded wafer sandwiches have the thickness of two wafers they have to be dressed to the proper size of 900 µm, which is the thickness of a standard wafer. A well defined amount of the PZT material has to be removed in a milling process from both sides of the sandwich. The ratio between top and bottom depends on the actuator type (200 dpi or 360 dpi). E.g., for a 200 dpi Chevron actuator the upper PZT layer has a thickness of 200 µm whereas the bottom layer is 700 µm. Fig. 6.3c illustrates this process step.

Inspection To reveal enclosed air pockets, particles or cracks, the sandwiches are inspected by shining a very bright light source through from the backside. Embedded features appear as dark spots whereas areas of good bonds are bright. Unfortunately, this techniques doesn't tell anything about the glue thickness and the homogeneity of the adhesive layer.

In addition to PZT-PZT sandwiches, PZT-glass sandwiches were produced. This was done mainly to get an idea on the amount and size distribution of embedded air pockets. Due to the transparency of the glass wafers the glue joint could be investigated with an optical microscope.

6.2.2 Optimization of active layer thicknesses

The ratio between top and bottom PZT layer in the Chevron sandwich is very important to achieve highly effective actuators. To find this ratio a number of simulations were performed using a *Xaar* internal software package specially developed for *Xaar*-type actuators. The output of the software is drop velocity and drop volume as functions of actuator geometry, driving voltage waveform and ink properties. Fig. 6.4 shows the simulation results for an XJ-128 Chevron actuator using standard wall geometry (including two PZT layers), waveform and ink. The optimal height of the top PZT layer is found to be between 45% and 50% of the total height.

To confirm this data a set of special actuators was made. During manufacturing the Chevron sandwich was slanted and in this way walls with top PZT layer ranging from 30% to 70% of the total height were achieved (Fig. 6.5).

The preparation of the slanted Chevron wafer is done in 3 steps.

1. Bonding of two standard PZT (900 µm height) wafers with polished surfaces in opposite polarization direction (Fig.6.6a);

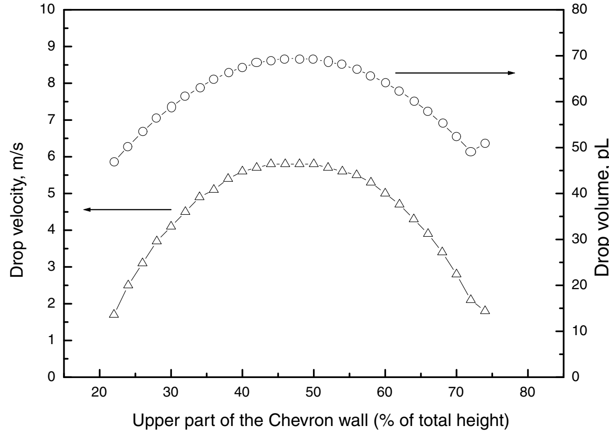

Figure 6.4. Simulation results for a slanted actuator having different ratio between the top and bottom half of the PZT sandwich. Optimal performance is expected when the top PZT layer is 45% to 50% of the complete wall height.

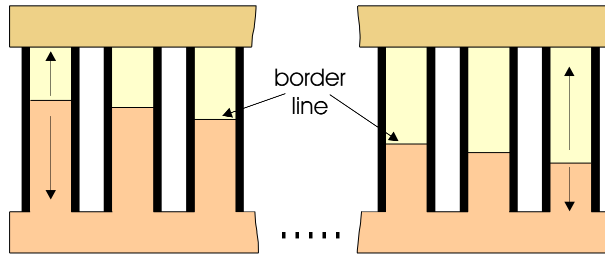

Figure 6.5. Arrangement of a slanted Chevron actuator to determine the best ratio between top and bottom PZT layer in the wafer sandwich.

2. Milling the wafer sandwich on a slanted chuck (wedge). The top wafer should have a residual height from 111 µm to 259 µm (Fig. 6.6b) (correspond 30% to 70% of the whole wall height);

3. Turning around the wafer sandwich and milling it to a thickness of 900 µm (standard channel wafer size) (Fig.6.6c and Fig. 6.6d);

Fig.6.6 displays in brief the manufacturing of the slanted Chevron.

The slanted Chevron sandwich was processed into actuators which were then characterized using an HP4194A Impedance Analyzer. Fig. 6.7 gives the measured admittance data. The obtained results agree very well with the simulation shown in Fig. 6.4. The optimal top/bottom ratio was identified to be between 45/55 to 50/50.

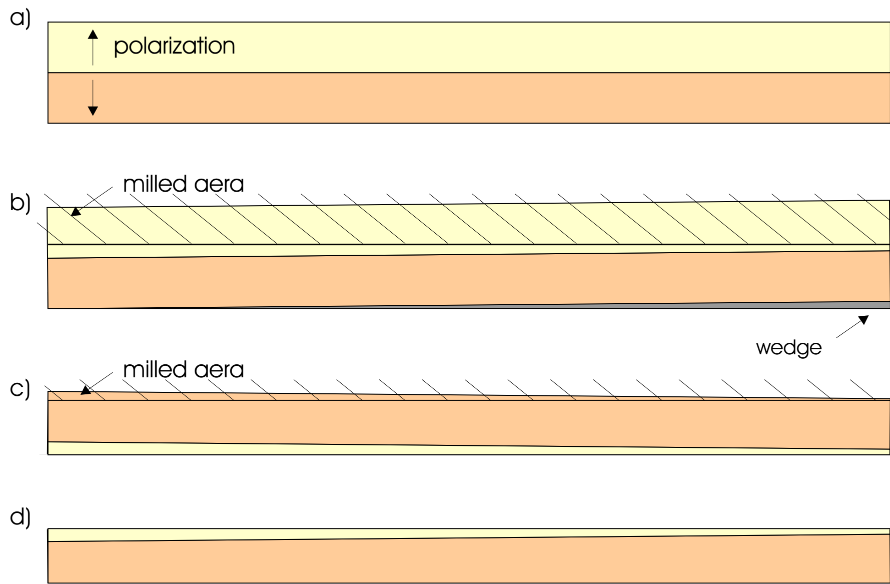

Figure 6.6. Production steps for making a slanted Chevron sandwich to determine the best top to bottom ratio of the laminated PZT layers.

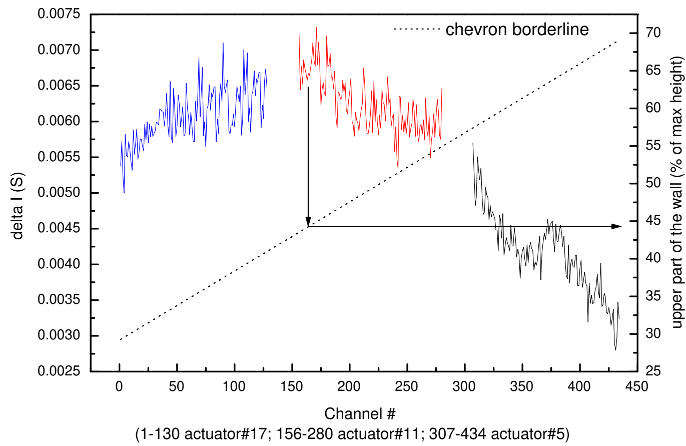

Figure 6.7. Measurement data for the slanted Chevron confirming the numbers obtained by simulations (see Fig. 6.5).

6.2.3 FEM simulations

The results of Finite Element Method (FEM) simulations of a Chevron channel wall is given in Fig. 6.8. In the simulations only a very simplified model of a Chevron wall is considered. Neither the rounding at the bottom of the wall nor the Si_3N_4 passivation are included to keep the computing time as short as possible. The highest deflection is found in the middle of the wall height which coincides very well with the data obtained for the slanted Chevron. Applying a voltage of 20 V yields a deformation of 66 nm. Simulations for a standard wall gave a maximum displacement of 26.6 nm as shown in Fig. 1.13.

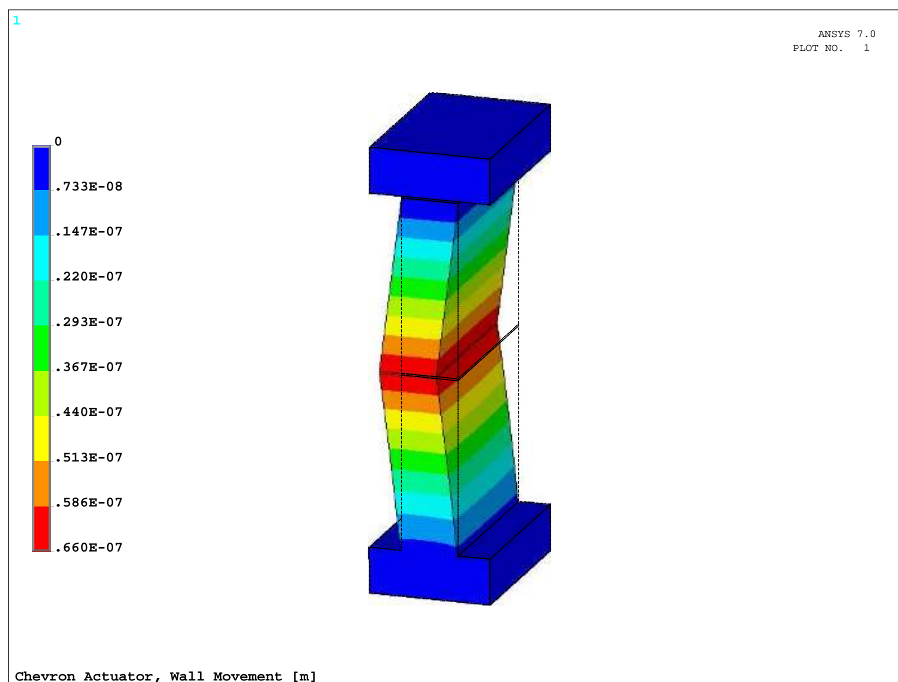

Figure 6.8. FEM analysis showing wall movement of a Chevron actuator

6.2.4 Influence of glue joint thickness

A series of experiments have been carried out to investigate the influence of the glue joint thickness on the performance of the Chevron actuator. It was found that thicker glue joints result in a change of resonance frequency of the channel wall. As long the joint has an equal thickness over the whole actuator the impact on the print performance is negligible. Only variations within the actuator can be seen as inhomogeneities in drop velocity. Fig. 6.9 shows an example for a 500 channels Chevron actuator with glue joint variations of up to 5 µm.

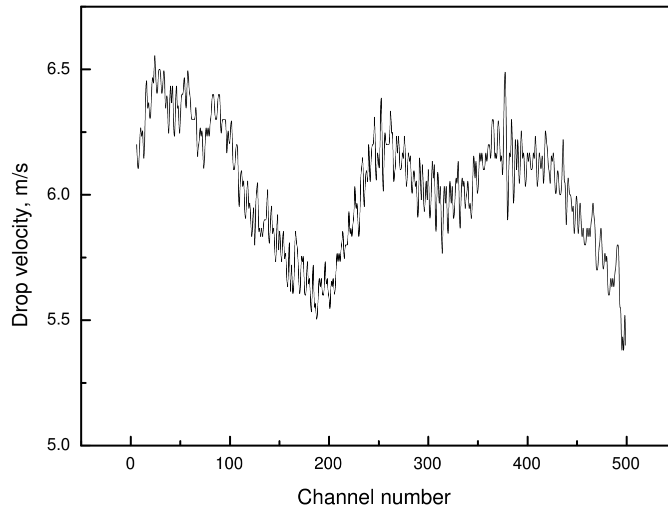

Figure 6.9. Drop velocity variation caused by non-uniform glue joint thickness

6.2.5 Alternative bonding method

An alternative way of preparing the Chevron sandwich is to use a so called *Bond Aligner* as known in the semiconductor industry (e.g. SB6 from Karl Suess). This process comprises good temperature control, well defined mechanical pressure for the bonding and, most important, the bonding can be performed in vacuum atmosphere. This could be a key element in making Chevron sandwiches without embedded air pockets. Until now only pre-studies have been carried out on this topic. Here, I would like to thank Prof. Stemme and Frank Niklaus from the S3/MST Department at KTH for their generous help and assistance.

6.3 Monolithic Chevron design

As described previously, making laminated Chevrons involves several machining steps and a gluing step which has to be performed in a cleanroom environment. An alternative method is the polarization reversal within the channel wall, which will be reviewed in the following section. No additional machining and gluing steps are needed for this approach which makes it interesting for high volume production.

6.3.1 Polarization set-up

For polarization reversal of a structured wafer there are two requirements:

- The application of an even DC-poling voltage of adequate amplitude to the wafer;
- The need to avoid damaging the sensitive channel structure of the wafer;

The fixture seen in Figs. 6.10 and 6.11 fulfils both conditions. It consists of a bottom (1) and a top (2) electrode and a sheet of conducting rubber (3) for electrical connection of the PZT wafer. The silver filled conductive rubber is pliable enough to conform to the channels. It is pressed onto the wafer surface by compressed air.

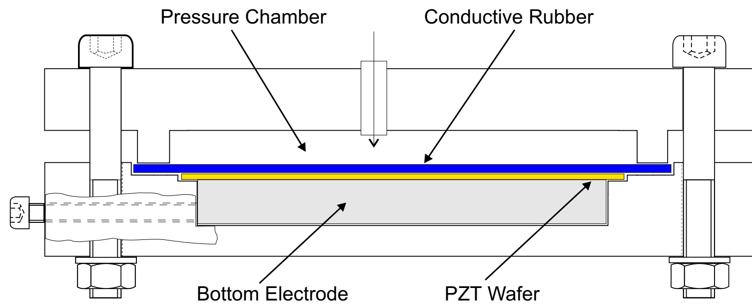

Figure 6.10. Schematic drawing of the fixture for polarization reversal.

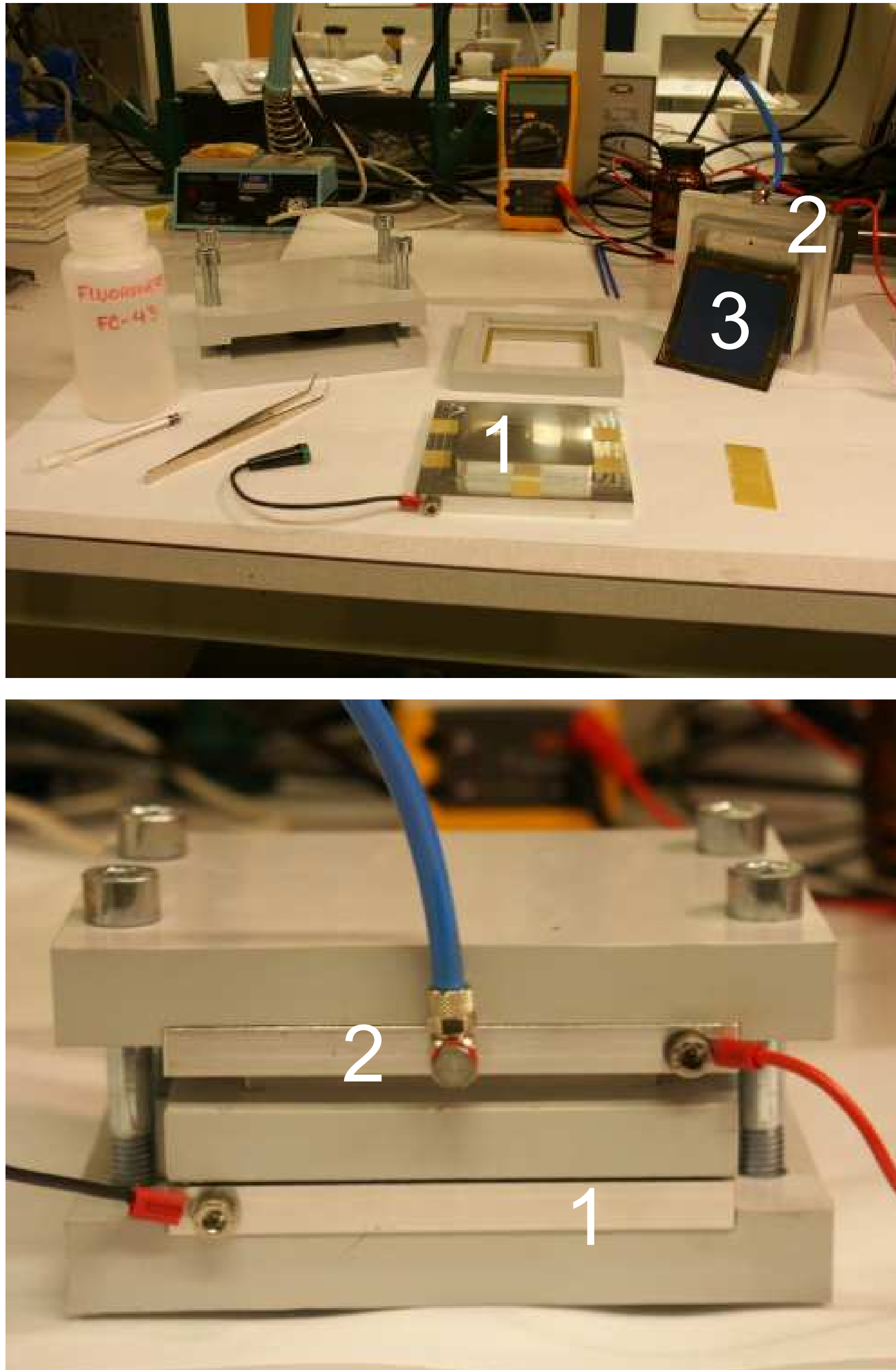

Figure 6.11. Poling Fixture: top) opened fixture, bottom) fixture ready for poling. The top electrode (2) is connected to the PZT wafer via an electrical conductive rubber (3) to avoid damages of the channel component.

6.3.2 Manufacturing

The base for the monolithic Chevron is a standard actuator and processing. After aluminium metallization (of half of the wall height) two additional steps to the standard process flow were introduced:

1. An electrical field higher than the coercive field E_c was applied between all the aluminium electrodes on the one side and the bottom of the channel wafer on the other side in order to reverse the poling direction at the lower half of the walls. The upper half of the walls is not influenced by the poling field due to the geometrical conditions of channels and their electrodes (see Fig. 6.12).

2. Depositing aluminium all over the channel height as it is done for the sandwich Chevron. After this the printhead is passed through the rest of the standard process flow.

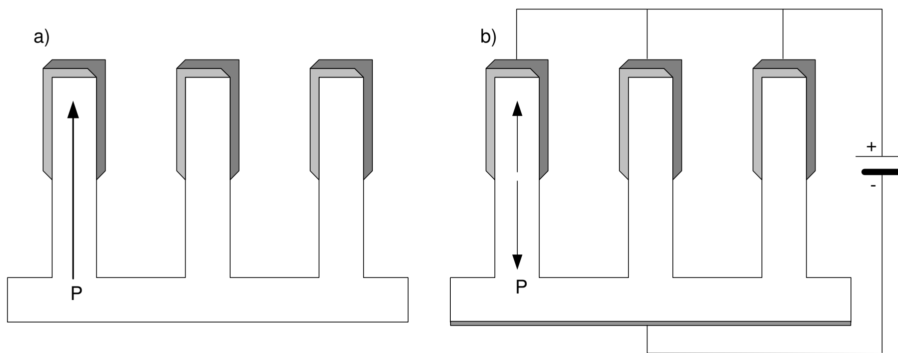

Figure 6.12. Polarization reversal of the lower part of the channel walls to implement a monolithic Chevron. The upper half of the walls with homogenous polarization a) are coated with aluminium electrodes. A poling voltage is applied between the aluminium electrodes and bottom electrode b). Only the polarization of the lower part of the wall is reversed because the aluminium electrodes short the upper parts.

The distribution of electric flux lines and therefore the theoretical evaluation of this approach is given by an ANSYS Finite Elements Method (FEM) simulation seen in Fig. 6.13.

In order to identify the optimal field strength for polarization reversal, a wafer was electrically separated into 9 areas (see Fig. 6.14) and electrical fields of different amplitude and different impact period were sampled this way. The electric field for poling reversal was chosen within the range 2100 to 2900 V/mm and the poling time was between 15 and 150 minutes.

When executing the poling reversal with high electric fields, snaps were audible. In order to avoid further snaps which could result in dielectric breakdown or at

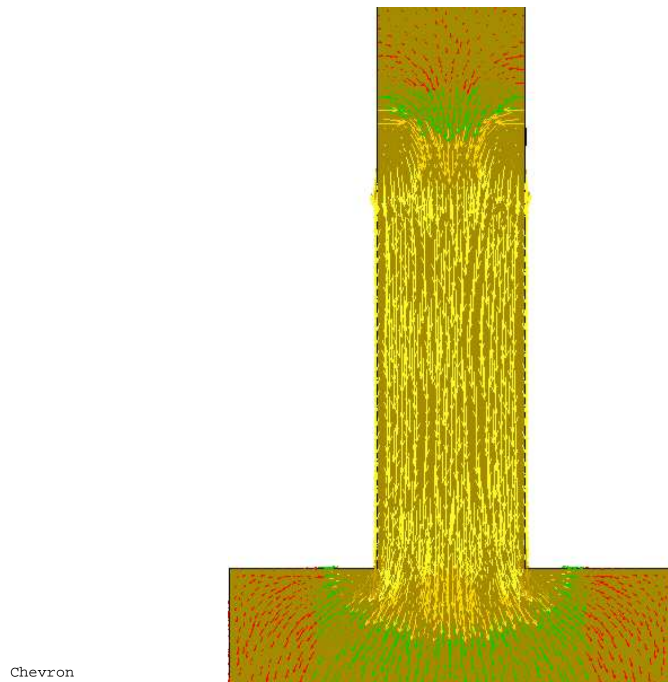

Figure 6.13. FEM simulation results for poling reversal fields. The lower half of the channel wall is displayed. The dashed line marks the height where the aluminium electrodes end. Image a) shows the electrical flux lines; image b) the equipotential lines.

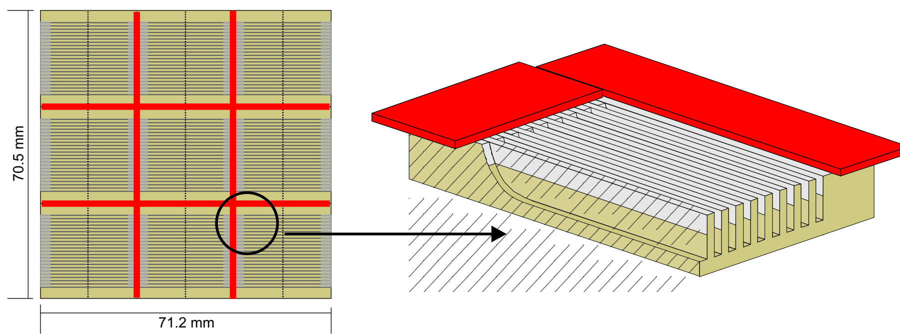

Figure 6.14. Specially prepared wafer for polarization reversal. For each of the 9 areas different electric poling fields were applied.

least in mechanical cracks, instead of the maximum electric field it was decided to apply the minimum field that is sufficient for:

a) reliable depoling of the original polarization (otherwise the actuator would definitely not work)

b) at least partial reverse poling

To determine this critical field strength, a DC-voltage oriented in the opposite direction to the original poling field and of rising amplitude was applied for one minute at a time. The capacitance was then measured after each of this steps. The measurements are shown in Fig. 6.15. Capacitance values were measured immediately after turning off the voltage. The values decreased with time, but this kind of measurement is sufficient to determine the critical field strength.

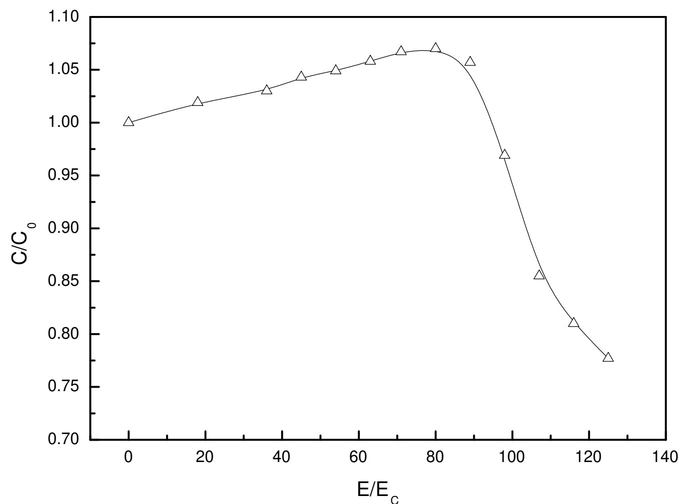

Figure 6.15. Turn up procedure of the voltage for polarization reversal

From 0 to 80% of the coercive field E_c the capacitance increased by approximately 8% due to non-remnant orientation of a few domains, which were oriented vertically to the poling field before. From 80% E_c, the capacitance drops and thus depolarization starts. At 125% E_c the capacitance minimum is reached because after applying 1.25 E_c a second time, the capacitance started to rise again. At this point it is clear that depolarization is finished and polarization in the inverse direction has been started. Trials with higher electrical fields show that even at 3 E_c a capacity of only 82% of the original polarization C_0 can be reached. This

is due to an area in the middle of the walls, where the poling direction remains undefined (see characteristics of flux lines in Fig. 6.13)

Only at poling reversal with the field strength marginally above the coercive field strength ($E = 1.25E_c$), as described above was a fully functional actuator achieved. Higher field strengths probably lead to micro cracks within the sawn channel structure due to the extreme enlargement of the poling field at the sharp edges of the deposited electrodes (see Fig. 6.13), which are unfavorable for the poling reversal. High electrical fields cause high mechanical stress within the PZT due to the inverse piezoelectric effect.

6.3.3 Functional performance

Functional performance of the actuators was investigated using stroboscopic analysis of ink drops in flight (see Chapter 3.5). The drop velocity, the drop volume and the angular deviation of the drops were measured for every channel. As seen in Fig. 6.16, the variations in drop velocity of the monolithic Chevron is as even as for the standard actuator. Both types of actuators have some channels at the ends, which have slower than average velocity.

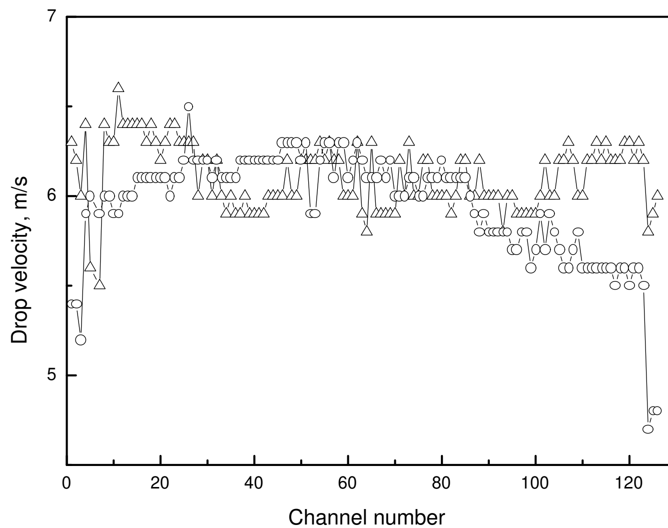

Figure 6.16. Distribution of drop velocity versus channel number for a monolithic Chevron actuator (△) and a standard actuator (○).

The variation of drop volume of the monolithic Chevron is higher and could be optimized to be more even (Fig. 6.17). The higher average volume suggests a

higher power efficiency. An interesting aspect is that in the case of the monolithic Chevron, most measurement points lie at the borders of the standard deviation (90 cf. 78 pl) and few points are near the average of 84 pl. Further investigations could show the reason for this effect.

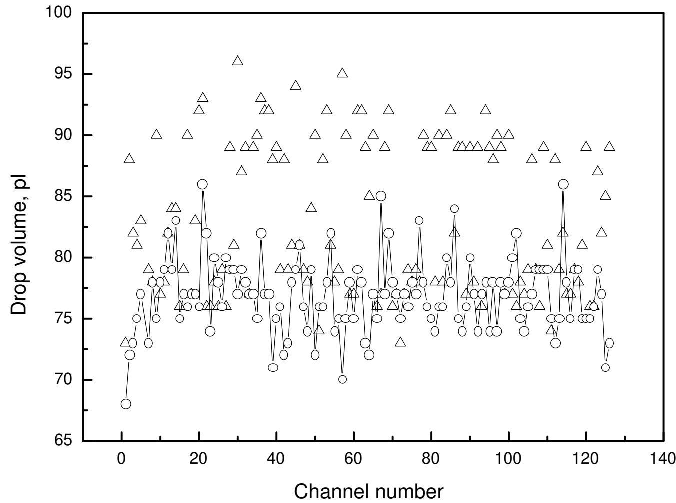

Figure 6.17. Distribution of drop volume versus channel number for a monolithic Chevron actuator (△) and a standard actuator (○).

The appropriate driving voltage for the monolithic chevron was identified as 20.5 Volts. Thus the power consumption of this Chevron-type printhead is reduced by approximately 20% compared to the corresponding standard Xaar XJ126-200 printhead, which has a driving voltage of approximately 25 Volts. The power efficiency increase of laminated chevron, which is up to 50%, cannot be reached with this actuator type due to a transition area of poling direction in the middle of the wall (see Fig. 6.13).

6.4 Conclusions

Two types of Chevron actuators have been made: Laminated Chevron and Monolithic Chevron. Pros and cons of both types are listed beneath in a short summary.

Laminated Chevron

+ power consumption of the printhead reduced by 50%;
+ improved homogeneity of the drop velocity within the actuator;
- good control of the glue layer thickness required;
- additional machining and gluing steps are necessary to produce the Chevron sandwich wafer;
- waste of expensive PZT material.

Monolithic Chevron

+ power consumption of the printhead reduced by 20% but less than the laminated Chevron with 50%;
+ just one additional metallization step is necessary and no extra machining of the PZT wafer is required;
- the ratio between top and bottom polarization part is dependent on the electrode depth after the first metallization;
- the mechanism of polarization reversal still not fully under control;
- time consuming process due to slow heating and cooling rate during polarization reversal.

Chapter 7

Summary of results

This section summarizes each appended paper and manuscript and also states the degree of my participation.

7.1 "Dielectric and Pulsed Spectroscopy of Shear Mode PZT Microactuator"

We examined the dielectric and mechanical properties of shear mode actuators. The measurements were done with an HP4194A Impedance Analyzer, a *Fluke* 6304 RCL meter, and a new pulsed technique, developed to characterize this type of actuators. Temperature dependencies of the properties were investigated as well.
My contribution
I prepared the samples, made the measurements and participated in the analysis and preparation of the manuscript.

7.2 "Non destructive Pulsed Technique to Characterize Functional Properties of Micromachined Bulk PZT"

This paper describes a non-destructive pulsed technique we have developed to characterize micromachined PZT ceramics. Dielectric properties and mechanical resonance behaviour of the actuators are measured and evaluated to obtain dielectric permittivity and losses, Curie temperature, mechanical quality factor, and resonance frequencies. Furthermore, we investigated fatigue in the PZT material due to high electric fields.

My contribution
I prepared the samples, made the measurements and participated in the analysis and preparation of the manuscript.

7.3 "Thermometry Inside Inkjet Actuators"

We present a new method to measure the temperature inside the inkjet actuators. In this technique 'dummy walls' located at the beginning and the end of a PZT channel wall array are used as sensing elements. Temperature changes inside the actuator will cause a change in the dielectric permittivity which can be measured as change in the capacitance of the 'dummy walls'. In this way we monitor the temperature at different printing conditions and in different printhead designs. More details are given in Chapter 5.
My contribution
I prepared parts of the samples, made measurements and participated in the analysis and preparation of the manuscript.

7.4 "Piezoelectric shear mode inkjet actuator"

This paper gives a survey of different printing techniques such as continuous jet, thermal jet and different techniques using piezoelectric actuators. More extensively the Xaar-type piezoelectric shear mode actuator is studied and characterized. Information about the manufacturing techniques are given. Characterizations that have been made are pulsed technique, ferroelectric hysteresis loop tracing and dielectric spectroscopy. The main resonance frequencies were found both by using dielectric spectroscopy and pulsed technique. Furthermore, PZT materials from different manufacturers were compared.
My contribution
I prepared the samples, made the measurements and the analysis and prepared the manuscript.

7.5 "Piezoelectric shear mode drop-on-demand inkjet actuator"

This review paper starts with an introduction into the field of inkjet printing by a brief description of the common technologies. We emphasize on *Xaar*-type shear mode actuators by giving details on their design and manufacturing methods. In the following we comprehensively characterize the actuators by dielectric and pulsed spectroscopy as well as ferroelectric hysteresis loop tracing and investigate the printing performance by stroboscopy. Furthermore, resonance characteristics of the actuators are investigated and analyzed.

My contribution
I prepared the samples, made the measurements and participated in the analysis and preparation of the manuscript.

7.6 ""Chevron"-type piezoelectric inkjet actuator"

We investigated resonance characteristics and functional performance of two types of inkjet actuators. Both types were based on the shared wall principle of *Xaar* inkjet printheads. In the standard type the channels walls have only one poling direction whereas in the Chevron-type the walls have two opposite directions of the polarization in the upper and lower halves of the wall. Fundamental resonances of the channel walls were detected by means of admittance spectroscopy with an HP4194A analyzer and a pulsed technique. Functional performance was tested by stroboscopic technique.
My contribution
I prepared the samples, made the measurements and the analysis and prepared the manuscript.

7.7 "Fatigue of shear mode PZT actuator"

Bulk wafers of polarized PZT ceramics were micromachined by sawing grooves with a high precision diamond saw to fabricate an array of channel walls. Stroboscopic tests were performed to quantify the ultimate inkjet performance: ink-drop velocity and volume. The temperature dependence of the dielectric permittivity was measured by an LCR meter and a novel pulsed technique. Ferroelectric hysteresis P-E loops were traced with a Sawyer-Tower circuit. The channel walls were subjected to electrical treatment (aging) by tracing of ferroelectric hysteresis P-E loops with a triangular shaped electric field. The high voltage treatment influences material properties (fatigue effect) seen in a change of the $P-E$ loops with the number of cycles. After 90,000 electric field cycles P_r decreased whereby E_c increased.
My contribution
I prepared the samples, made the measurements and participated in the analysis and preparation of the manuscript.

Bibliography

[1] F. R. S. Rayleigh. On the instability of jets. *Proc. London Math. Soc.*, **10**(4):4–13, 1878.

[2] R. Elmqvist. Measuring instrument of the recording type. U.S. Patent no. 2,566,443, 1948.

[3] R.G. Sweet. Signal apparatus with fluid drop recorder. U.S. Patent no. 3,596,275, 1971.

[4] W. L. Buehner, J. D. Hill, T. H. Williams, and J. W. Woods. Application of ink-jet technology to a word processing output printer. *IBM J. Res. Dev.*, **21**:2–9, 1977.

[5] S. L. Zoltan. Pulse droplet ejection system. U.S. Patent no. 3,857,049, Clevite Corp., 1974.

[6] I. Endo, Y. Sato, S. Saito, T. Nakagiri, and O. Ohno. Liquid jet recording process and apparatus therefor. Great Britain Patent no. 2,007,162, Canon, 1979.

[7] J. L. Vaught, F. L. Cloutier, D. K. Donald, J. D. Meyer, C. A. Tacklind, and H. H. Taub. Thermal ink-jet printer. U.S. Patent no. 4,491,728, Hewlett-Packard, 1984.

[8] H. P. Le. Progress and trends in ink-jet printing technology. *Journal of Imaging Science and Technology*, **42**:42–62, 1998.

[9] F. J. Kampfhoefner. Ink-jet printing. *IEEE Trans. Elec. Devices*, ED**19**:584, 1972.

[10] L. Kuhn and A. Myers. Ink-jet printing. *Scientific America*, **240**:162–178, 1979.

[11] W. Wehl. Nur nicht kleckern. *CHIP*, **8**:104–112, 1994.

[12] H. H. Taub and P. H. Wolf. Ink jet head structure. U.S. Patent no. 4,306,243, DataProducts Corp., 1918.

[13] T. Goldman and J. S. Gonzales. DNA-printing: utilization of a standard inkjet printer for the transfer of nucleic acids to solid supports. *J. Biochem. Biophys. Methods*, **42**:105–110, 2000.

[14] G. Percin, T. Lundgren, and B. Khuri-Yakub. Controlled ink-jet printing and deposition of organic polymers and solid particles. *Appl. Phys. Lett*, **73**:No.16, 1998.

[15] W. Voit, K. V. Rao, and W. Zapka. Direct-write process for UV-curable epoxy materials by inkjet technology. page LL3.5.1. in Mat. Res. Soc. Symp. Proc. **758**.

[16] W. G. Hawkins. Bubble jet priniting device. U.S. Patent no. 4,523,530, Xerox Corp., 1985.

[17] E. L. Kyser and S. B. Sears. Method and apparatus for recording with writing fluids and drop projection means therefor. U.S. Patent no. 3,946,398, Siliconics Inc., 1976.

[18] A. Mikalesen. Apparatus and method employing phase change ink. U.S. Patent no. 4,742,364, DataProducts Corp., 1988.

[19] W. S. Bartky, A. D. Paton, S. Temple, and A. J. Michaelis. Droplet deposition apparatus. U.S. Patent no. 4,879,568, Xaar, 1989.

[20] G. Beurer and J. Kretschmer. Function and performance of a shear mode piezo printhead. In *International Conference on Digital Printing Technologies NIP **13***, pages 621–625. IS&T, October 1997.

[21] H. J. Manning and R. A. Harvey. Xaar greyscale technology. In *International Conference on Digital Printing Technologies NIP **15***, pages 35–39. IS&T, October 1999.

[22] http://www.epson.com.

[23] http://www.xaar.co.uk. April, 17th 2003.

[24] Rolf Kaack. Large drop actuators. Master's thesis, University of Freiburg, Germany, July 2001.

[25] N. Aurell, D. Roche, C. Richard, and P. Gonnard. Sample aspect ratio influence on the shear coefficients measurements of a piezoelectric bar. In *Proceedings of the Ninth IEEE International Symposium on Applications on Ferroelectrics*, pages 162–165. ISAF '94/IEEE, 1994.

[26] A. Ballato. Piezoelectricity: Old effect, new thrust. *IEEE Transactions on Ultrasonics, Ferroelectrics and Frequency Control*, **42**:916–926, 1995.

[27] J. R. Phillips. Piezoelectirc technology primer. Technical report, CTS Wireless Components.

[28] Yuhuan Xu. *Ferroelectric materials and their applications.* North-Holland, 1991.

[29] Standrad on piezoelectricity. ANSI/IEEE Standard 176-1987, 1988.

[30] Standrad definitions and methods of measuring for piezoelectric vibrators. ANSI/IEEE Standard 177, 1966.

[31] C. M. Harris and C. E. Crede. *Shock and Vibration Handbook.* Chapter 7. McGraw-Hill, New York, 4th edition, 1995.

[32] M. E. Lines. *Principles and applications of ferroelectrics and related materials*, page 102. Oxford University Press, Clarendon, 1977.

[33] Jürgen Brünahl. Incorporating a PZT thermosensor into a XaarJet printhead for on-line temperature compensation. Master's thesis, Fachhochschule Zweibrücken, Germany, 1999.

[34] A. Jorzick and W. Zapka. Real-time temperature measurement inside a printhead actuator. In *The Eigth International Conference on new Actuators, Actuator 2002*, pages . 138–140, 2002.

[35] Thomas Jäger. Investigation and characterization of special ink-jet actuators. Master's thesis, Albert-Ludwigs-University of Freiburg, Germany, 2002.

Index

acoustic
- compression wave, 13
- periode, 13
- rarefaction wave, 13

actuator
- bend mode, 9
- Chevron-type, *see* Chevron
- push mode, 9
- shear mode, 11
- squeeze mode, 8

admittance, 35
angular deviation, 15, 83
ANSYS, 19

base plate, 11, 69
bend mode, *see* actuator
bonding, 72
Bubble-Jet, 7

capacitance, 34, 59
Chevron, 69
- active layer, 73
- alternative bonding, 77
- glue joint, 73
- laminated, 71
  - FEM, 76
  - glue joint, 77
  - manufacturing, 71
- monolithic
  - design, 78
  - FEM, 80
  - manufacturing, 80
- slanted, 73

coercive field, 27, 82
conductive rubber, 78
coupling coefficient, 28, 37, 38
cover bonding, 14
cover plate, 11, 69
- AlN, 65

Curie temperature, 14, 23, 28, 48, 60
Curie-Weiss
- constant, 28
- law, 28, 47

d_{15}, *see* piezoelectric coefficient
depolarization, 82
design
- shear mode, 11

dicing, 14
dielectric
- constant, 27, 59, 60
- loss, 27, 33, 47, 48
- permittivity, 27, 33, 47, 48
- spectroscopy, 33, 47, 48

dipol, 24
- reorientation, 50
- rotation, 50

domain, 24
- boundary, 24

dpi, 15
dressing, 73
driving voltage, 12, 58, 84
drop
- generation, 12
- lead-, 42
- satellite-, 42
- velocity, 15, 18, 43, 57, 83
- volume, 15, 17, 43, 83

dummy channel, 58, 61
dY, 37

electrode, 69
electrodes, 12, 13

Fast Fourier Transform, *see* FFT
fatigue, 50
FEM, 19
ferroelectric, 28
    fatigue, *see* fatigue
FFT, 39
Finite Element Method, *see* FEM
Fluke PM6304, 33, 47

HP4194 Impedance Analyser, 35
HP4194A Impedance Analyzer, 48, 53, 74
hysteresis, 26, 50
    measurement, 40

impedance, 34, 35
ink
    channels, 11
    inlet, 12, 63
inkjet
    continuous, 6
    drop-on-demand, 7
    history, 5
    piezoelectric, 8
    thermal, 7

lamination, 72
lead zirconate titanate, *see* PZT

manufacturing
    shear mode, 13
MEMS, 7, 23
metallization, 13
    Chevron, 80

nozzle
    diameter, 19
    plate, 12
nozzle plate, 14

paraelectric, 28
passivation, 14, 76
phase transition, 28
piezoelectic
    piezoelectricity, 29
piezoelectric
    coefficient, 17, 29
    directions, 29
    effect, 17, 23, 29, 36, 38
    inverse effect, 23, 36
polarization, 26, 50, 82
    Chevron, 71
    direction, 12
    microscope, 50
    remnant, 26, 27, 50
    reversal, 78, 80
    set-up, 78
    standard, 69
poling, 26
    de-, 26
    direction, 80
    electrodes, 26
    field, 26
    field strength, 82
polishing, 72
power consumption, 69, 85
pressure in channel, 16
pulsed spectroscopy, 38, 47, 48, 53
push mode, *see* actuator
PZT, 11, 23, 30
    history, 23
    machining, 13

quality factor, 34

reactance, 34
resistance, 34
resolution, 15
resonance
    acoustic modes, 53
    analysis, 19
    frequency, 19, 35, 38, 39, 48, 53
        parallel, 37
        serial, 37
    test, 35

Sawyer-Tower circuit, 40

shear
  displacement, 12, 30
  strain, 31
squeeze mode, *see* actuator
Stroboscopy, 42
stroboscopy, 55, 83

tanδ, *see* dielectric loss
temperature
  compensation, 57, 58
  sensor, 57
thermal conductivity, 65
thermistor, 58
thermometry, 57

viscosity, 57
voltage divider circuit, 61

Xaar actuator, *see* shear mode

Appendix A

PZT piezoelectric materials technical data